



## Full Length Article

Highly porous single-phase rhombohedral  $\text{Cr}_x\text{Rh}_{2-x}\text{O}_3$  nanofibers expediting oxygen evolution reaction

Taehui Kwon <sup>a,1</sup>, Kyungmin Kim <sup>a,1</sup>, Sampath Prabhakaran <sup>b,1</sup>, Subin Choi <sup>a</sup>, Jiwon Kim <sup>a</sup>, Yeji Yim <sup>a</sup>, Jihyun Park <sup>c</sup>, Hoi Ri Moon <sup>a</sup>, Myung Hwa Kim <sup>a,\*</sup>, Do Hwan Kim <sup>b,\*</sup>, Youngmi Lee <sup>a,\*</sup>

<sup>a</sup> Department of Chemistry & Nanoscience, Ewha Womans University, Seoul, 03760, Republic of Korea

<sup>b</sup> Division of Science Education, Institute of Fusion Science, Graduate School of Department of Energy Storage/Energy Conversion Engineering, Jeonbuk National University, Jeonbuk, 54896, Republic of Korea

<sup>c</sup> Department of Chemistry, Ulsan National Institute of Science and Technology (UNIST), Ulsan, 44919, Republic of Korea



## ARTICLE INFO

## Keywords:

Rhombohedral  $\text{CoRhO}_3$   
Oxygen evolution reaction (OER)  
Electrospinning  
Nanofiber  
Density functional theory (DFT) simulation

## ABSTRACT

Single-phase rhombohedral  $\text{Cr}_x\text{Rh}_{2-x}\text{O}_3$  nanofibers are demonstrated as an excellent and stable electrocatalyst for oxygen evolution reaction (OER) under alkaline condition. Facile optimization of the annealing temperature for electrospun nanofibers composed of Cr/Rh metal precursors and poly(vinylpyrrolidone) could produce highly porous nanofibers of single-phase  $\text{Cr}_x\text{Rh}_{2-x}\text{O}_3$  by randomly distributing two metal ions of  $\text{Cr}^{3+}$  and  $\text{Rh}^{3+}$  in the rhombohedral crystalline lattice sites. Single-phase  $\text{Cr}_x\text{Rh}_{2-x}\text{O}_3$  could then induce the best synergistic effect of Cr and Rh owing to the perturbation of the surface electronic structure of the electrocatalyst active site and much enlarged electroactive surface area. Density functional theory (DFT) simulation integrated with experimental data indicated that the increased activity was due to moderate *d*-band center energy levels. This regulates oxygen desorption and adsorption capacities in the intermediates (\*OH, \*O, and \*OOH). Conclusively,  $\text{Cr}_x\text{Rh}_{2-x}\text{O}_3$  nanofibers exhibited superior OER catalytic performances (low overpotential and Tafel slope with high stability and easy product desorption) compared to other Rh-related catalysts reported to date.

## 1. Introduction

As a clean energy source, hydrogen is presented as an important alternative and has the advantages of abundant stockpiles, sustainability, and eco-friendliness. Hydrogen production through electrochemical water splitting is considered as one of the sustainable zero-carbon emission strategies, compared to the typical vapor formation or coal gasification based on the reaction between fossil fuels and steam [1–3]. However, it is still difficult to achieve high-efficiency hydrogen production on an industrial scale using renewable energy. Essentially, the oxygen evolution reaction (OER) at the anode as a half-cell reaction of the water electrolyzer has much slower kinetics than the hydrogen evolution reaction at the cathode due to the slow four-electron transfer process of the OER [4–7]. Thus, the development of cost-effective electrocatalysts to accelerate the sluggish kinetics of OER with enhanced durability is an important step toward realizing this goal.

Generally, rutile-structured Ru and Ir oxides have been known as state-of-the-art electrocatalysts that considerably improve the electrocatalytic performances for OER [8–12]. However, their practical applications still suffer from their limited resources, prohibitive cost of noble metal, and poor durability [13]. To address the aforementioned limitations, tremendous strategies have been developed for more efficient utilization of precious metals while improving OER catalyst activity and stability and reducing precious metal usage. The existing strategies can be classified into two major types: (1) adjusting the morphology of catalyst to expose more active sites, such as nanoparticles/nanoframes [14–17], nanotubes/nanoneedles [18,19], and nanosheets [20,21]; and (2) altering the electronic structure of the catalyst to control intermediate adsorption, which in turn improves the intrinsic activity of each active site, including a mixed phase or solid solution with first-row transition metals (Ni, Co, Cu, and Cr, etc.) [22–26]. Common sense is that the surface electronic structure is a major factor influencing the

\* Corresponding authors.

E-mail addresses: [myungkim@ewha.ac.kr](mailto:myungkim@ewha.ac.kr) (M.H. Kim), [dhk201@jbnu.ac.kr](mailto:dhk201@jbnu.ac.kr) (D.H. Kim), [youngmilee@ewha.ac.kr](mailto:youngmilee@ewha.ac.kr) (Y. Lee).

<sup>1</sup> These authors equally contributed to this work.

catalytic activity, and in particular, the incorporation of heteroatoms can control the intrinsic electronic structure of the electrocatalyst active site [27].

Particularly, Cr has recently attracted more attention as a potential electrode material for OER [28], due to its various attainable redox states ( $\text{Cr}^0$ ,  $\text{Cr}^{2+}$ ,  $\text{Cr}^{3+}$  and  $\text{Cr}^{6+}$ ) and substantial abundance in the earth's crust [29]. Cr is also a critical component of stainless steel, which is used as the current collector in alkaline electrolyzers [30]. In light of several studies applying Cr as an electrocatalytic component, it is clear that pure Cr is generally considered catalytically inert due to its low electronic conductivity but Cr contributes indirectly to the observed activity [30,31]. To the best of our knowledge, only a few nanomaterials fabricated with a combination of Cr and noble metal have been reported, in an attempt to circumvent the cost and complexity of electrocatalytic components [25,26,32]. Thus, a better understanding of the physico-chemical properties of the Cr-based electrocatalysts and their development using a facile synthetic methodology are still challenging.

In this paper, we demonstrate, for the first time, the synthesis of single-phase rhombohedral structured  $\text{Cr}_x\text{Rh}_{2-x}\text{O}_3$  porous nanofibers by electrospinning and following calcination step and scrutinize their electrochemical performances as a promising electrocatalyst for effective OER in alkaline condition. In general, electrospinning is a remarkably simple and versatile technology, and is currently considered one of the most fascinating directions for the manufacture of low-dimensional nanostructures with various morphologies [33–35]. By simply modifying annealing temperature, we successfully synthesized single-phase nanomaterials having optimal electronic synergistic effect between Cr and Rh ions, and figured out how elaborate condition affects porous structures (e.g., pore size) that maximize the benefits of electrospinning technology. Density functional theory (DFT) analysis indicates that  $\text{CrRhO}_3$  can intensify the charge distribution and elevate the density of states (DOS) near the Fermi level, thus consequently increasing  $\text{CrRhO}_3$ 's energy level. Since OER overpotentials are strongly related to the energy level of the *d*-band center ( $\epsilon_d$ ) [36], a moderate increase in the energy levels induces this trend while balancing the oxygen-containing intermediates' adsorption and desorption capacities ( $^*\text{OH}$ ,  $^*\text{O}$ , and  $^*\text{OOH}$ ). Therefore, the significantly improved OER activity of single-phase rhombohedral electrospun  $\text{Cr}_x\text{Rh}_{2-x}\text{O}_3$  suggests our synthetic methodology applicable to new materials as an effective OER electrocatalyst.

## 2. Experimental

### 2.1. Materials

Chromium(III) chloride hexa-hydrate ( $\text{CrCl}_3 \cdot 6\text{H}_2\text{O} \geq 98.0\%$ ), rhodium(III) chloride hydrate ( $\text{RhCl}_3 \cdot x\text{H}_2\text{O} \geq 99.9\%$ ), poly(vinylpyrrolidone) (PVP, MW  $\approx 1300,000$ ), potassium hydroxide (KOH), potassium hexacyanoferrate (III), potassium chloride and Nafion (5 wt % solution) were purchased from Sigma-Aldrich (St. Louis, MO, USA). *N,N*-dimethyl-formamide (DMF, extra pure grade) was purchased from DUKSAN (Korea). Commercial iridium (Ir/C, 20 wt % Ir loaded on Vulcan XC-72) was purchased from Premetek Company. All aqueous solutions were prepared using deionized water (resistivity  $\geq 18\text{ M}\Omega\cdot\text{cm}$ ).

### 2.2. Synthetic methods of $\text{Cr}_x\text{Rh}_{2-x}\text{O}_3$ nanofibers

$\text{Cr}_x\text{Rh}_{2-x}\text{O}_3$  nanofibers were synthesized through electrospinning and subsequent heat treatment. 20.9 mg of rhodium precursor ( $\text{RhCl}_3 \cdot x\text{H}_2\text{O}$ , 0.1 mM) and 26.6 mg of chromium precursor ( $\text{CrCl}_3 \cdot 6\text{H}_2\text{O}$ , 0.1 mM) were added to 2.2 mL of a mixed solvent (DMF: deionized water = 1.2:1) and completely dissolved by 10 min of sonication. 300 mg of PVP was added to the solution and stirred at 450 rpm for 17 h for stabilization. The prepared homogeneous mixture was placed in a plastic syringe, connected to a needle tip, and mounted on an

electrospinning device (Nano NC ESR200R2). The distance between the needle tip and collector was adjusted to 11 cm where a voltage of 12.5 kV was applied and the precursor solution radiated through the needle at a speed of  $7\ \mu\text{L}\ \text{min}^{-1}$ . The collected spun-fibers were heated to four different targeted temperatures (400, 450, 500 and 550 °C) at a rate of  $10\ ^\circ\text{C}\ \text{min}^{-1}$  and maintained for 1 h and 30 min under a condition where He and  $\text{O}_2$  flow 90 sccm and 5 sccm, respectively. For comparison, chromium oxide and rhodium oxide, which were single metal oxides, were synthesized in the same manner using only one metal precursor (either  $\text{CrCl}_3 \cdot 6\text{H}_2\text{O}$  or  $\text{RhCl}_3 \cdot x\text{H}_2\text{O}$ ) with an annealing temperature of 450 °C.

### 2.3. Physical characterization

Morphologies, physical structures and chemical compositions of the synthesized nanofibers were characterized by using inductively coupled plasma-atomic emission spectroscopy (ICP-AES; Perkin-Elmer OPTIMA 8300), X-ray diffraction (XRD; Rigaku D/Max-2000/PC X-ray diffractometer using  $\text{Cu}\ \text{K}\alpha$  radiation), field-emission scanning electron microscopy (FE-SEM; JOEL JSM-7610F equipped with energy dispersive X-ray spectrometer (EDS)), high-resolution transmission electron microscopy (HR-TEM; JEOL JEM-ARM 200F NEOARM) equipped with selected area electron diffraction (SAED) micrographs and energy dispersive X-ray spectroscopy (EDS) mapping and angle-resolved X-ray photoelectron spectrometer (XPS). Nitrogen adsorption-desorption isotherm was obtained utilizing a BELSORP-max instrument at a temperature of 77 K.

### 2.4. Electrochemical measurements

Electrochemical measurements were performed using a three-electrode system on a CHI920C electrochemical station (CH Instruments). A Pt wire and a saturated calomel electrode (SCE) were used as the counter electrode and reference electrode, respectively. The catalyst ink was prepared by dispersing each prepared catalyst in deionized water to a concentration of  $2\ \text{mg}\ \text{mL}^{-1}$ .  $6\ \mu\text{L}$  each of the well-dispersed samples was loaded on a glassy carbon (GC, diameter: 3 mm) disk electrode and dried for 10 min at 60 °C in an oven. This process was repeated five times to load  $60\ \mu\text{g}$  of each synthesized nanomaterial in total. Then,  $10\ \mu\text{L}$  of 0.1 wt % Nafion (diluted in ethanol) was added dropwise onto the modified-GC electrode and dried in an oven for 10 min. A GC rotating disk electrode (RDE) loaded with each sample was used as the working electrode. All the potentials in SCE scale were converted to reversible hydrogen electrode (RHE) scale potentials to remove the pH effect and corrected with *iR*-compensation (100 %). To measure the catalytic activities toward the OER, RDE voltammetry was carried out using an electrochemical analyzer (RDE-1 rotor/Epsilon electrochemical analyzer, BASi) in Ar-saturated 1.0 M KOH aqueous (aq) solution at a rotation rate of 1600 rpm. Cyclic voltammetry (CV) tests were performed in a non-faradaic potential range of 0.2 V in 1.0 M KOH (aq) solution to estimate the capacitive currents of the catalysts. Electrochemical impedance spectroscopy (EIS) was conducted in 1.0 M KOH (aq) solution at a potential of 1.517 V (vs RHE) in the frequency range from 0.01 Hz to 1 kHz. Each of the OER polarization curves was normalized to the electrode geometric surface areas (GSAs). The GSAs were obtained with chronocoulometry (CC) experiments in 0.1 M KCl solution containing 10 mM  $\text{K}_3[\text{Fe}(\text{CN})_6]$  [37].

### 2.5. Computational methods

According to the XRD results, we carefully examined the electrocatalyst and its crystalline structure via density functional theory (DFT) calculations using Vienna ab initio Simulation Package (VASP) [38,39]. The Perdew–Burke–Ernzerhof (PBE) exchange-correlation functional was applied along with Grimme's DFT-D3 functional with a semi-empirical GGA type theory [40]. The projector augmented wave

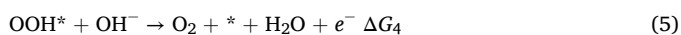
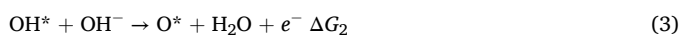
method (PAW) was implemented in VASP for ion-electron interactions [41]. To prevent the atom interaction between neighboring slabs, vacuum layer of 16 Å was applied in the Z direction. Plane-wave basis set 520 eV was fixed as cut-off energy. The  $2 \times 2 \times 1$  supercell was constructed and relaxed totally until the Hellman-Feynman forces were lower than  $0.02 \text{ eV \AA}^{-1}$ . For Brillouin zone sampling, a  $\Gamma$ -centered  $7 \times 2 \times 1$  k-point mesh was employed, offering sufficient accuracy for surface slab calculations and capturing the system's anisotropic periodicity.

The formation energy ( $E_f$ ) is defined as in Eq. (1) below:

$$E_f = E^* - \sum_i n_i E_i \quad (1)$$

where  $E^*$ ,  $n_i$  and  $E_i$  represent the energy of every crystal structure, the number of the elements in the crystal, the energy of each constituting element, respectively.

For the OER calculation, a four electron-mechanism was used to simplify the OER process. Based on the following reactions the OER mechanism can be expressed:



where  $\text{OH}_{\text{ads}}$ ,  $\text{O}_{\text{ads}}$ ,  $\text{OOH}_{\text{ads}}$  are intermediate species adsorbed on the active sites of catalyst and  $\Delta G_1$ ,  $\Delta G_2$ ,  $\Delta G_3$ , and  $\Delta G_4$  are Gibbs free energy changes in each reaction step. The change in Gibbs free energy ( $\Delta G$ ) in each of the reaction steps (2) to (5) is determined using Eq. (6).

$$\Delta G = \Delta E + \Delta \text{ZPE} - T\Delta S - neU + \Delta G(\text{pH}) \quad (6)$$

$\Delta E$  value is calculated using the energy of the catalyst with oxygen species.  $\Delta \text{ZPE}$  and  $\Delta S$  denote changes in zero-point energy and entropy, respectively.  $T$  represents temperature under standard conditions 298.15 K,  $P = 1 \text{ bar}$ ,  $\text{pH} = 0$ . In addition, the term  $-neU$  is often used to correct the bias effect involved in electron transfer, where  $U$  denotes electrode potential.  $\Delta G(\text{pH}) = \Delta kT \ln([\text{H}^+])$  is a free energy correction term based on  $\text{H}^+$  ion concentration. Theoretical overpotentials ( $\eta$ ) of all considered structures were calculated by the following equation [42, 43].

$$\eta_{\text{OER}} = \frac{\max\{\Delta G_1, \Delta G_2, \Delta G_3, \Delta G_4\}}{e} - 1.23(\text{V}) \quad (7)$$

where  $\max\{\Delta G_1, \Delta G_2, \Delta G_3, \Delta G_4\}$  denotes the Gibbs energy change in the elementary step.

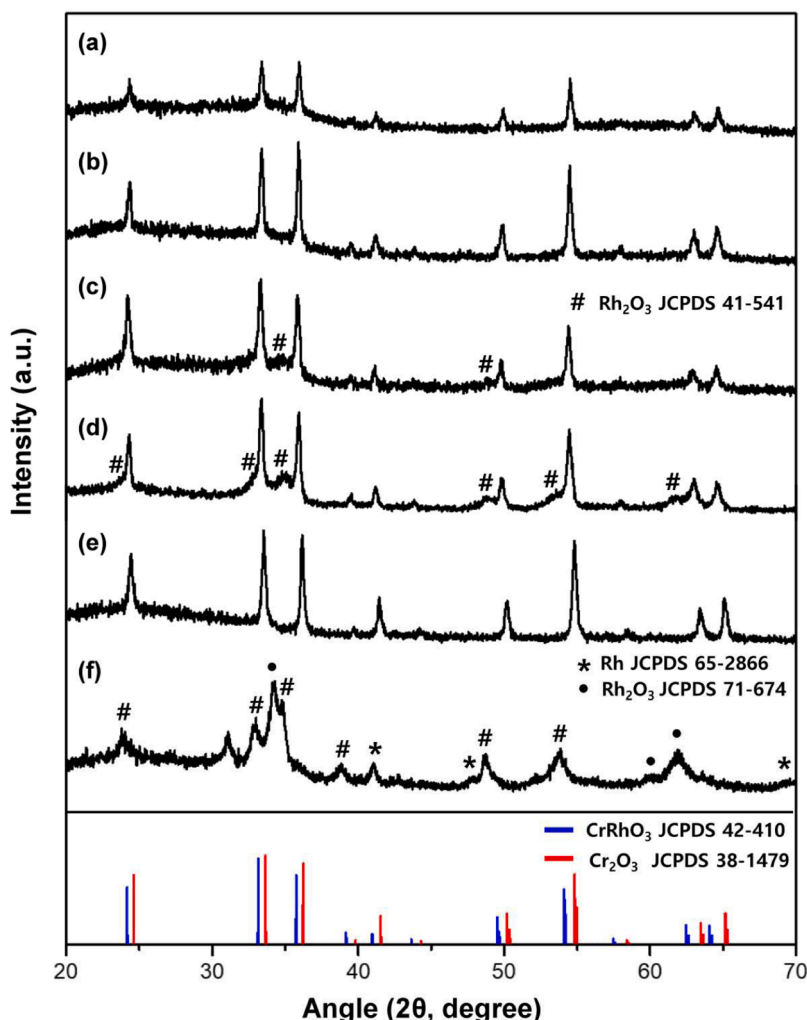


**Fig. 1.** XRD patterns of the as-prepared catalysts: (a)  $\text{Cr}_x\text{Rh}_{2-x}\text{O}_3$ -400, (b)  $\text{Cr}_x\text{Rh}_{2-x}\text{O}_3$ -450, (c)  $\text{Cr}_x\text{Rh}_{2-x}\text{O}_3$ -500, (d)  $\text{Cr}_x\text{Rh}_{2-x}\text{O}_3$ -550, (e)  $\text{Cr}_2\text{O}_3$  and (f)  $\text{RhO}_3$ . Representative patterns for  $\text{CrRhO}_3$ ,  $\text{Cr}_2\text{O}_3$ ,  $\text{Rh}_2\text{O}_3$ , and Rh from the JCPDS database are provided for comparison.

### 3. Results and discussion

#### 3.1. Physical characterization

Cr-Rh binary metal oxides were synthesized through a facile electrospinning and subsequent heat treatment at a series of temperatures between 400 and 550 °C. For clarity, in this work, the as-prepared Cr-Rh alloy metal oxides were denoted as  $\text{Cr}_x\text{Rh}_{2-x}\text{O}_3\text{-}T$ , where  $T$  is the corresponding annealing temperature in °C (i.e., 400, 450, 500 and 550). The crystal structures were verified with XRD technique. Fig. 1 shows the diffraction peaks of Cr-Rh binary metal oxides calcined at different temperatures and single metal oxides (denoted as  $\text{Cr}_2\text{O}_3$  and  $\text{RhO}_y$ ) synthesized at 450 °C. All the XRD patterns of  $\text{Cr}_x\text{Rh}_{2-x}\text{O}_3\text{-}T$  were well indexed to the pure rhombohedral  $\text{CrRhO}_3$  (JCPDS 42–410), while an additional impurity phase was found in  $\text{Cr}_x\text{Rh}_{2-x}\text{O}_3\text{-}500$  and  $-550$ . The eight distinct diffraction peaks of  $\text{Cr}_x\text{Rh}_{2-x}\text{O}_3\text{-}T$  at 24.1°, 33.1°, 35.7°, 40.9°, 49.5°, 54.1°, 62.5°, and 64.1° were assigned to (012), (104), (110), (113), (024), (116), (214), and (300) planes of  $\text{CrRhO}_3$ , which were barely observed for alloy metal oxides produced at lower annealing temperature, 350 °C (Fig. S1). The diffraction peaks of  $\text{Cr}_x\text{Rh}_{2-x}\text{O}_3\text{-}400$  showed particularly weaker intensity than those of the other  $\text{Cr}_x\text{Rh}_{2-x}\text{O}_3\text{-}T$  materials, suggesting the declined crystallinity owing to the decreased annealing temperature [44–46]. The XRD spectrum of  $\text{Cr}_x\text{Rh}_{2-x}\text{O}_3\text{-}450$  clearly showed the peaks corresponding to  $\text{CrRhO}_3$  without other miscellaneous peaks, supporting the successful formation of highly pure rhombohedral  $\text{CrRhO}_3$  phase (Fig. 1b). For  $\text{Cr}_x\text{Rh}_{2-x}\text{O}_3\text{-}500$ , the additional small peaks appeared at 35.0° and 53.4° corresponding to (110) and (012) planes of  $\text{Rh}_2\text{O}_3$  rhombohedral phase (JCPDS 41–541).  $\text{Cr}_x\text{Rh}_{2-x}\text{O}_3\text{-}550$ , annealed at even higher temperature, exhibited more distinct peaks at 23.8°, 32.8°, 35.0°, 48.72°, 53.4°, and 61.5° being assigned to (116), (104), (110), (024), (012) and (214) planes of  $\text{Rh}_2\text{O}_3$  rhombohedral phase (JCPDS 41–541). Note that all the peaks of rhombohedral  $\text{CrRhO}_3$  are slightly shifted to higher diffraction angles toward the locations of rhombohedral  $\text{Cr}_2\text{O}_3$  peaks (JCPDS 38–1479) as shown in Fig. 1a-d and Fig. S2. Given that  $\text{Cr}^{3+}$  ion (75.5 pm) is absolutely smaller than  $\text{Rh}^{3+}$  ion (80.5 pm), it is reasonable to accept that the blue-shifted peaks indicate the presence of greater amount of Cr than Rh in the  $\text{CrRhO}_3$  phase [47], also confirmed with EDS analyses (*vide infra*). The XRD spectrum of pure  $\text{Cr}_2\text{O}_3$  in Fig. 1e corresponded to  $\text{Cr}_2\text{O}_3$  rhombohedral structure consistent with the reference values (JCPDS 38–1479), indicating the well-synthesized single phase at the same thermal oxidation condition. As shown in Fig. 1f, the diffraction patterns of  $\text{RhO}_y$  calcined at 450 °C exhibited complex features with predominant peaks at 23.8°, 32.8°, 35.0°, 38.9°, 48.7° and 53.4° corresponding to (116), (104), (110), (113), (024) and (012) planes of rhombohedral  $\text{Rh}_2\text{O}_3$  phase (JCPDS 41–541). In addition,  $\text{RhO}_y$  presented small peaks at 41.1°, 47.8° and 69.9° assigned to (111), (200) and (220) of  $\text{Rh}(0)$  metal cubic phase (JCPDS 65–2866) and other peaks at 34.2°, 60.0° and 62.1° associated with (114), (220) and (200) planes of orthorhombic  $\text{Rh}_2\text{O}_3$  phase (JCPDS 71–674). This clearly demonstrates that the electrospun pure Rh oxide calcined at 450 °C exist in a mixture form of two different phases of  $\text{Rh}_2\text{O}_3$  and a tiny amount of  $\text{Rh}(0)$  metal. In contrast, binary oxide alloys formed with Cr metal precursors at the same annealing temperature as 450 °C exist as a single rhombohedral phase of  $\text{CrRhO}_3$  without any by-product. Since the ionic size of  $\text{Cr}^{3+}$  and  $\text{Rh}^{3+}$  in the formation of  $\text{CrRhO}_3$  is not much different, it is reasonably suggested that Rh ions prefer to be randomly incorporated into  $\text{Cr}_2\text{O}_3$  rather than to be presented as segregated single oxides or metal under precisely controlled conditions. Moreover, the incorporation of Rh ions into  $\text{Cr}_2\text{O}_3$  structures might cause the structural distortion in the synthesized  $\text{Cr}_x\text{Rh}_{2-x}\text{O}_3\text{-}T$ ; and these structural defects could enhance OER performance by increasing active sites for electrochemical catalysis, as previously reported [48–50]. In addition, the crystallite sizes of  $\text{Cr}_2\text{O}_3$  and  $\text{Cr}_x\text{Rh}_{2-x}\text{O}_3\text{-}T$  were calculated based on Scherrer equation [ $D = K\lambda/(\beta \cdot \cos\theta)$ ], where  $D$  is the mean size of the crystalline domains,  $K$  is the Scherrer constant,  $\lambda$  is the wavelength of X-ray,  $\beta$  is the

peak full width at half maximum in radians, and  $\theta$  is the Bragg angle] applied to the (104) plane for all materials [51]. The estimated crystallite sizes were 31.9, 30.7, 23.7, 28.6, and 28.6 nm for  $\text{Cr}_2\text{O}_3$ ,  $\text{Cr}_x\text{Rh}_{2-x}\text{O}_3\text{-}400$ ,  $\text{Cr}_x\text{Rh}_{2-x}\text{O}_3\text{-}450$ ,  $\text{Cr}_x\text{Rh}_{2-x}\text{O}_3\text{-}500$ , and  $\text{Cr}_x\text{Rh}_{2-x}\text{O}_3\text{-}550$ , respectively. It suggests that the annealing temperature and the incorporation of  $\text{Rh}^{3+}$  ions influence the crystallite sizes of  $\text{Cr}_2\text{O}_3$  host. It should be noted that the synthesis of single rhombohedral  $\text{CrRhO}_3$  structure has not ever been reported previously since the X-ray diffraction data of the rhombohedral framework, first studied in 1961 by Khanolkar [52], especially none using electrospinning techniques.

In the SEM images (Fig. 2), all  $\text{Cr}_x\text{Rh}_{2-x}\text{O}_3\text{-}T$  materials showed fibrous structures consistently but different surficial roughness depending on the thermal oxidation temperature, while as-spun materials were very smooth nanofibers (Fig. S3). Due to a rather low annealing temperature insufficient for the complete PVP decomposition,  $\text{Cr}_x\text{Rh}_{2-x}\text{O}_3\text{-}400$  exhibited a relatively larger diameter than the other  $\text{Cr}_x\text{Rh}_{2-x}\text{O}_3\text{-}T$  nanofibers (Table S1). Both  $\text{Cr}_x\text{Rh}_{2-x}\text{O}_3\text{-}400$  and  $\text{Cr}_x\text{Rh}_{2-x}\text{O}_3\text{-}450$  revealed the smooth surfaces. Contrastively, the surficial morphology of  $\text{Cr}_x\text{Rh}_{2-x}\text{O}_3\text{-}500$  and  $\text{Cr}_x\text{Rh}_{2-x}\text{O}_3\text{-}550$  was rough, indicating that aggregated nanoparticles seemed to exist porously on the surface of nanofibers (Fig. 2c and d).  $\text{RhO}_y$  showed the smooth fibrous shape, and  $\text{Cr}_2\text{O}_3$  exhibited a collapsed tube-like shape in which small-sized nanoparticles formed through excessive self-aggregation were continuously connected. Based on the EDS results, all  $\text{Cr}_x\text{Rh}_{2-x}\text{O}_3\text{-}T$  materials were similarly composed of a little higher Cr content than Rh even though the electrospinning precursor solution contained the equal atomic contents of Cr and Rh (Table S2). The molar ratio of Cr: Rh for  $\text{Cr}_x\text{Rh}_{2-x}\text{O}_3\text{-}450$  was measured to be 53.5: 46.5 from ICP-AES analysis (Table S3), well matched with the composition measured by EDS.

The detailed crystal structure and morphology of  $\text{Cr}_x\text{Rh}_{2-x}\text{O}_3\text{-}T$  were characterized using HRTEM, as shown in Fig. 3 and Fig. S4. Interestingly, the TEM images showed that the nanofibers, observed as very smooth ones in the SEM image, were formed with nicely packed nanoparticles having an average diameter of about 3 nm (Fig. 3a). HRTEM image and the corresponding fast Fourier transform (FFT) clearly indicated the high crystallinity of  $\text{Cr}_x\text{Rh}_{2-x}\text{O}_3\text{-}450$  (Fig. 3b). The  $d$ -spacing values of 0.250, 0.3677 and 0.1691 nm, measured from the lattice resolved HRTEM image, approximately corresponded to the (110), (012), and (116) lattice planes of rhombohedral  $\text{CrRhO}_3$  unit cell, respectively. The slight difference compared with those calculated from the reference  $\text{CrRhO}_3$  (JCPDS 42–410) [52] is ascribed to the difference in the unit cell size, consistent with the XRD peak shifts in Fig. S2. In Fig. 3c, EDS mapping data confirm that Cr, Rh, and O atoms are uniformly distributed through the entire  $\text{Cr}_x\text{Rh}_{2-x}\text{O}_3\text{-}450$  nanofiber. To further investigate the impact of calcination temperature on the porous surface structure of the nanofibers generated via nanoparticle packing, the TEM images for  $\text{Cr}_x\text{Rh}_{2-x}\text{O}_3\text{-}T$  (Fig. S4) were analyzed to determine the pore sizes which were plotted as a function of the annealing temperature (Fig. S5). These estimated values reveal that the pore sizes of  $\text{Cr}_x\text{Rh}_{2-x}\text{O}_3\text{-}T$  with  $T \geq 450$  have a linear correlation with the annealing temperature, suggesting more aggregation to form larger nanoparticles at higher annealing temperature [53]. Generally, an elongated fibrous structure can provide high conductivity for electron transport [54]. Besides, its porous surface structure has a high specific surface area, which is additionally advantageous for obtaining high electrocatalytic activities.

To support these estimations, the porosity and BET surface area of the  $\text{Cr}_x\text{Rh}_{2-x}\text{O}_3\text{-}450$  and  $-500$  exhibiting the highest catalytic activity were analyzed as shown in Fig. S6 and Table S4. The  $\text{N}_2$  adsorption-desorption isotherms for both  $\text{Cr}_x\text{Rh}_{2-x}\text{O}_3\text{-}450$  and  $\text{Cr}_x\text{Rh}_{2-x}\text{O}_3\text{-}500$  exhibited the combination of type I and type IV isotherms of the IUPAC classification, indicating the presence of both micropore and mesopore structures. The average pore diameters for  $\text{Cr}_x\text{Rh}_{2-x}\text{O}_3\text{-}450$  and  $\text{Cr}_x\text{Rh}_{2-x}\text{O}_3\text{-}500$  were measured to be 1.54 nm and 3.47 nm, respectively, from BET analysis using BJH method. These sizes are in good agreement with the sizes estimated by HR-TEM analysis (1.11 nm and

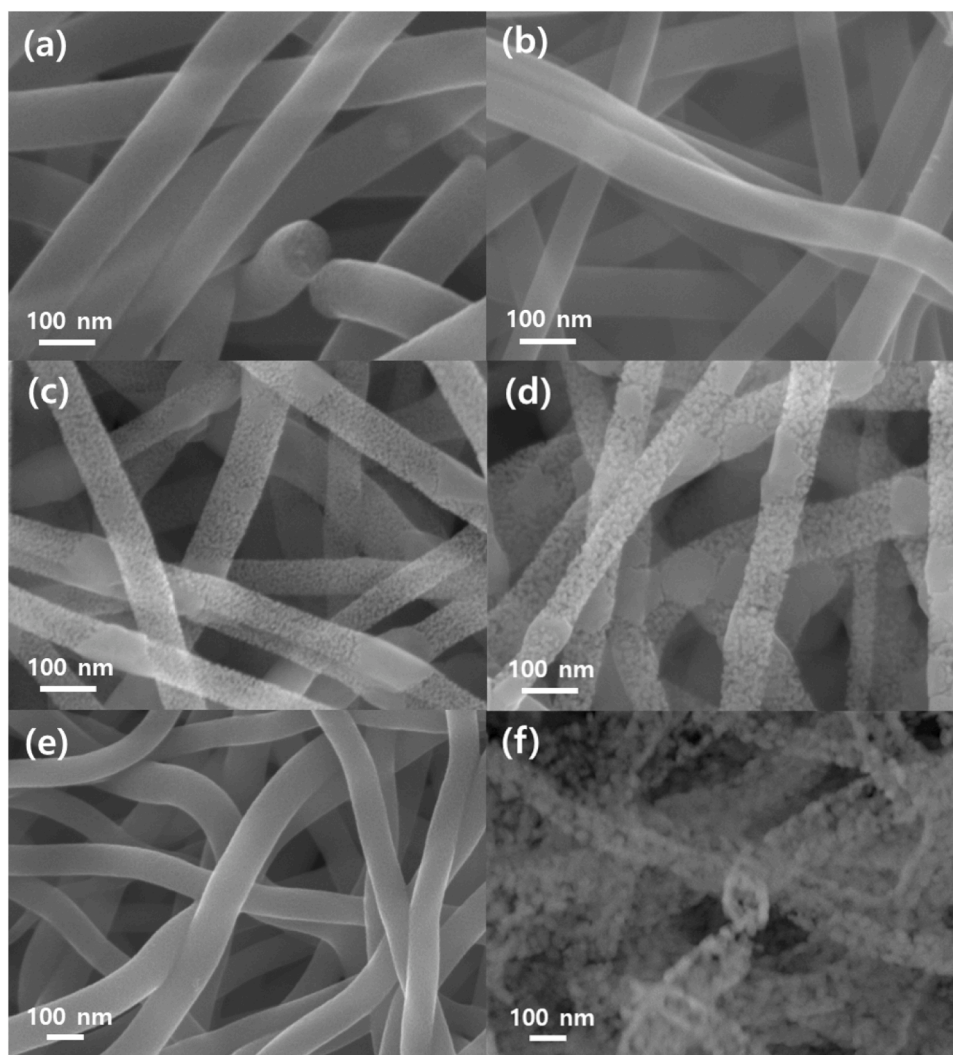


**Fig. 2.** FE-SEM images of Cr-Rh binary metal oxides and single metal oxides: (a)  $\text{Cr}_x\text{Rh}_{2-x}\text{O}_3$ -400, (b)  $\text{Cr}_x\text{Rh}_{2-x}\text{O}_3$ -450, (c)  $\text{Cr}_x\text{Rh}_{2-x}\text{O}_3$ -500, (d)  $\text{Cr}_x\text{Rh}_{2-x}\text{O}_3$ -550, (e)  $\text{RhO}_y$ , and (f)  $\text{Cr}_2\text{O}_3$ .

3.61 nm), thereby confirming the smaller pore size of  $\text{Cr}_x\text{Rh}_{2-x}\text{O}_3$ -450. Additionally, the BET surface area of  $\text{Cr}_x\text{Rh}_{2-x}\text{O}_3$ -450 was found to be  $318.47 \text{ m}^2 \text{ g}^{-1}$ , which is more than double that of  $\text{Cr}_x\text{Rh}_{2-x}\text{O}_3$ -500. This increase in the surface area leads to a greater exposed reactive surface, thereby explaining the enhanced OER activity of  $\text{Cr}_x\text{Rh}_{2-x}\text{O}_3$ -450 despite its comparable total pore volume to  $\text{Cr}_x\text{Rh}_{2-x}\text{O}_3$ -500.

Fig. 4 shows the high resolution XPS spectra of  $\text{Cr}_x\text{Rh}_{2-x}\text{O}_3$ -450. The low-resolution survey spectrum in Fig. 4a shows that only Cr, O, and Rh without other elemental traces clearly exist on the surface of the  $\text{Cr}_x\text{Rh}_{2-x}\text{O}_3$ -450 evidencing the high purity. The Cr 2p XPS spectrum (Fig. 4b) shows two prominent peaks around 586 eV and 576 eV, which are typical split spin-orbit Cr  $2p_{1/2}$  and Cr  $2p_{3/2}$ , respectively, for the  $\text{Cr}^{3+}$  in  $\text{Cr}_2\text{O}_3$  [55]. In fact, the  $\text{Cr}^{3+}$   $2p_{3/2}$  peak was deconvoluted to five constituent peaks. Multiplet splitting occurs when atom has an unpaired electron such as  $\text{Cr}^{3+}$ , because the unpaired electron in the outer shell can be coupled with that of the core shell caused by photoionization, resulting in various final states [55]. The binding energies and relative areas of Cr  $2p_{3/2}$  five constituent peaks were very close to the reference values of  $\text{Cr}^{3+}$   $2p_{3/2}$  in  $\text{Cr}_2\text{O}_3$  as shown in Table S5 [55]. Since none of these five peaks were similarly positioned to either Cr(0)  $2p_{3/2}$  (574.2 eV) or  $\text{Cr}^{4+}$   $2p_{3/2}$  (579.0 eV), Cr atoms in  $\text{Cr}_x\text{Rh}_{2-x}\text{O}_3$ -450 were considered to have an oxidation state of +3 [56]. Rh 3d doublet peaks at 313.2 eV and 308.4 eV in Fig. 4c were consistent with the  $\text{Rh}^{3+}$   $3d_{3/2}$  and  $3d_{5/2}$ , respectively [57]. These peak positions are very close to the

standard peaks of  $\text{Rh}_2\text{O}_3$  (313.2 eV for  $3d_{3/2}$  and 308.5 eV for  $3d_{5/2}$ ), but different from those of metallic Rh (311.7 eV for  $3d_{3/2}$  and 307.0 eV for  $3d_{5/2}$ ) [57]. This demonstrates that Rh in  $\text{Cr}_x\text{Rh}_{2-x}\text{O}_3$  is present as  $\text{Rh}^{3+}$ , substituting some  $\text{Cr}^{3+}$  sites of  $\text{Cr}_2\text{O}_3$ . In Fig. 4d, O 1s peak at 529.8 eV corresponded to a typical peak of oxygen directly bonded to metal in the lattice, and a broad shoulder peak located at about 531.3 eV was related to oxygen present on the surface, such as hydroxide and moisture from the environment [58]. XPS analyses along with XRD and HRTEM measurements consistently support that  $\text{Cr}_x\text{Rh}_{2-x}\text{O}_3$ -450 forms a single rhombohedral phase  $\text{CrRhO}_3$  where Cr and Rh elements are present as  $\text{Cr}^{3+}$  and  $\text{Rh}^{3+}$ . A comparison of the chemical states of  $\text{Cr}_x\text{Rh}_{2-x}\text{O}_3$ -450 with the single metal oxides ( $\text{Cr}_2\text{O}_3$  and  $\text{RhO}_y$ ) are shown in Fig. S7. The Cr 2p core-level XPS profiles, which consist of distinct doublets induced by spin-orbit splitting corresponding to the  $2p_{3/2}$  and  $2p_{1/2}$  states for pure  $\text{Cr}_2\text{O}_3$  and  $\text{Cr}_x\text{Rh}_{2-x}\text{O}_3$ -450 nanofibers, clearly showed that the peak positions for  $\text{Cr}_x\text{Rh}_{2-x}\text{O}_3$ -450 nanofibers were slightly shifted to higher binding energies compared to those of pure  $\text{Cr}_2\text{O}_3$  nanofibers, with shifts of 1.2 eV for the Cr  $2p_{1/2}$  state and 0.3 eV for the Cr  $2p_{3/2}$  state, respectively. This indicates that the charge state of Cr ions in  $\text{Cr}_x\text{Rh}_{2-x}\text{O}_3$ -450 nanofibers is more positive than that of pure  $\text{Cr}_2\text{O}_3$  nanofibers due to the partial substitution of  $\text{Rh}^{3+}$  ions for  $\text{Cr}^{3+}$  ion sites in the rhombohedral structure of  $\text{Cr}_2\text{O}_3$ . Based on the electronegativity difference (Cr: 1.66 and Rh: 2.28), it is reasonably expected that Cr is less effective at attracting electron density compared to Rh in

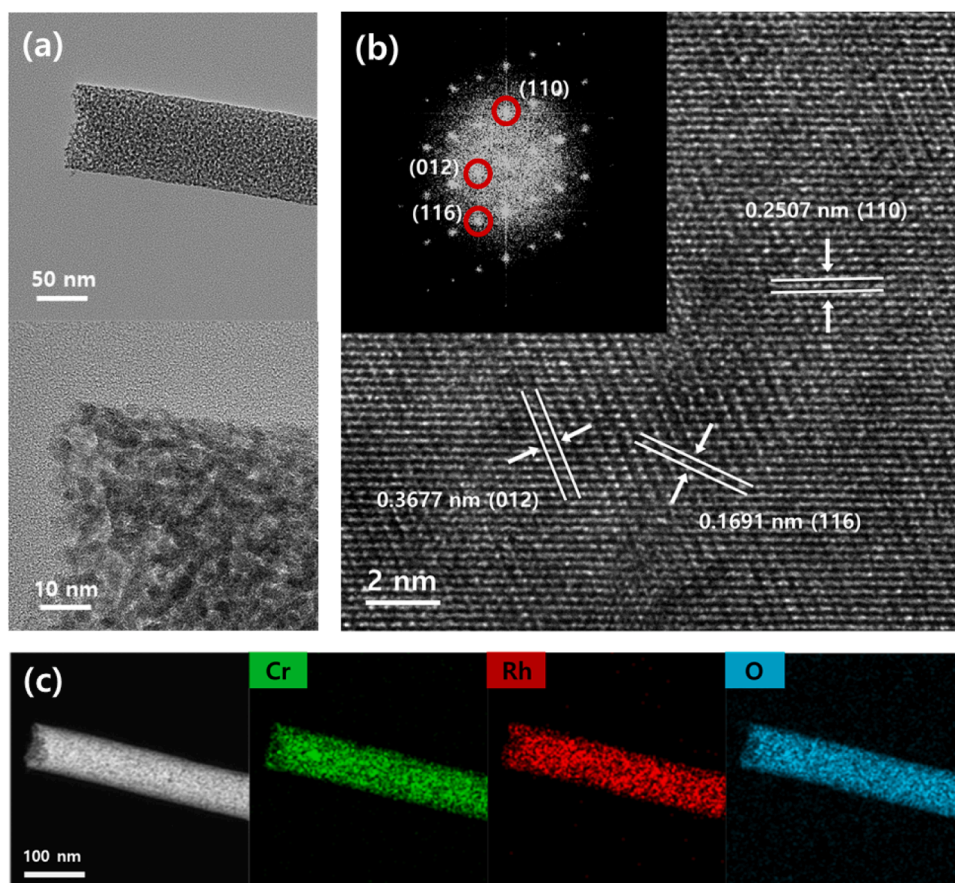


**Fig. 3.** (a) Low magnification TEM images and (b) HRTEM image of  $\text{Cr}_x\text{Rh}_{2-x}\text{O}_3\text{-450}$ . The inset shows the FFT of the lattice resolved image. (c) Elemental mapping analysis of Cr, Rh and O atoms in  $\text{Cr}_x\text{Rh}_{2-x}\text{O}_3\text{-450}$ .

$\text{Cr}_x\text{Rh}_{2-x}\text{O}_3\text{-450}$ , leading to the shifts of the peak positions of XPS 3p states toward higher binding energies compared to pure  $\text{Cr}_2\text{O}_3$ . In contrast, the peak positions for the Rh 3d XPS spectra for both  $\text{RhO}_y$  and  $\text{Cr}_x\text{Rh}_{2-x}\text{O}_3\text{-450}$  nanofibers are nearly identical. This is likely because a pure  $\text{Rh}_2\text{O}_3$  phase could not be synthesized under the same synthetic conditions. Indeed, XRD analysis (Fig. 1f) confirms the coexistence of metallic Rh and  $\text{Rh}_2\text{O}_3$  phases in  $\text{RhO}_y$  nanofibers. Therefore, it is thought that the Rh 3d XPS peaks of  $\text{RhO}_y$  nanofibers appear at lower binding energies than those of pure  $\text{Rh}_2\text{O}_3$  and are similar to the binding energies observed for the peaks observed for  $\text{Cr}_x\text{Rh}_{2-x}\text{O}_3\text{-450}$  nanofibers, where the electron density around  $\text{Rh}^{3+}$  ions becomes slightly higher due to the interaction with  $\text{Cr}^{3+}$  ions.

### 3.2. Electrochemical characterization for OER

The OER activity of the prepared materials was performed in a strong alkaline solution (1.0 M KOH). Fig. 5a shows the linear sweep voltammetry (LSV) curves with RDE voltammetry. Notably, all  $\text{Cr}_x\text{Rh}_{2-x}\text{O}_3\text{-T}$  nanofibers showed the greater OER catalytic performances compared with those of single metal oxides ( $\text{Cr}_2\text{O}_3$  and  $\text{RhO}_y$ ). In particular,  $\text{Cr}_x\text{Rh}_{2-x}\text{O}_3\text{-450}$  exhibited the lowest onset potential ( $\sim 1.43$  V vs RHE,  $\sim 200$  mV overpotential) among the tested materials. Additionally, overpotential to achieve a current density of  $10 \text{ mA cm}^{-2}$  ( $\eta_{10}$ ) was also the smallest (255 mV) for  $\text{Cr}_x\text{Rh}_{2-x}\text{O}_3\text{-450}$ :  $\eta_{10}$  values were 301, 289, 326, 1044, and 333 mV for  $\text{Cr}_x\text{Rh}_{2-x}\text{O}_3\text{-400}$ ,  $\text{Cr}_x\text{Rh}_{2-x}\text{O}_3\text{-500}$ ,  $\text{Cr}_x\text{Rh}_{2-x}\text{O}_3\text{-550}$ ,  $\text{Cr}_2\text{O}_3$ , and  $\text{RhO}_y$ , respectively. Even compared to the state of the art electrocatalyst, Ir/C,  $\text{Cr}_x\text{Rh}_{2-x}\text{O}_3\text{-450}$  showed 34-mV lower  $\eta_{10}$ . The favorable catalysis was much more pronounced at higher current density.  $\text{Cr}_x\text{Rh}_{2-x}\text{O}_3\text{-450}$  required only 308-mV overpotential (1.538 V vs RHE) to attain a current density of  $50 \text{ mA cm}^{-2}$ .

However,  $\text{RhO}_y$  and Ir/C only generated much smaller current density of 5, 19  $\text{mA cm}^{-2}$ , respectively, at the same potential. It emphasizes the highest OER electrocatalytic activity of  $\text{Cr}_x\text{Rh}_{2-x}\text{O}_3\text{-450}$  among the examined materials (Fig. 5b and Table S6). In fact, the OER activity decreased upon increasing the annealing temperature above  $450^\circ\text{C}$  as seen in Fig. S8. It presents a volcano shape, suggesting that  $450^\circ\text{C}$  is the optimal annealing temperature among the  $\text{Cr}_x\text{Rh}_{2-x}\text{O}_3\text{-T}$  nanomaterials. Tafel plots derived from the voltammetric curves using the Tafel equation [ $\eta = b \log j + a$ , where  $\eta$  is the overpotential,  $j$  is the current density, and  $b$  is the Tafel slope] [59] are presented in Fig. 5c. The Tafel slopes were calculated to be  $60.3 \text{ mV dec}^{-1}$  for  $\text{Cr}_x\text{Rh}_{2-x}\text{O}_3\text{-450}$ ,  $68.3 \text{ mV dec}^{-1}$  for  $\text{Cr}_x\text{Rh}_{2-x}\text{O}_3\text{-500}$ , and  $67.2 \text{ mV dec}^{-1}$  for  $\text{Cr}_x\text{Rh}_{2-x}\text{O}_3\text{-550}$ , revealing the much improved OER kinetics (*i.e.*, smaller Tafel slope) of  $\text{Cr}_x\text{Rh}_{2-x}\text{O}_3\text{-T}$  compared to that of  $\text{RhO}_y$  ( $76.3 \text{ mV dec}^{-1}$ ). As aforementioned,  $\text{Cr}_x\text{Rh}_{2-x}\text{O}_3\text{-400}$  showed relatively slower OER kinetics (*i.e.*, relatively larger Tafel slope) due to its carbon residue. The Tafel slopes and  $\eta_{10}$  values of the materials (Table S6) showed that  $\text{Cr}_x\text{Rh}_{2-x}\text{O}_3\text{-T}$  synthesized at  $T \geq 450^\circ\text{C}$  had better OER catalytic activity (lower overpotentials and smaller Tafel slopes) than pure metal oxides. The apparently worse OER performances of  $\text{Cr}_x\text{Rh}_{2-x}\text{O}_3\text{-500}$  and  $\text{Cr}_x\text{Rh}_{2-x}\text{O}_3\text{-550}$  among  $\text{Cr}_x\text{Rh}_{2-x}\text{O}_3\text{-T}$  series could be attributed to the presence of  $\text{Rh}_2\text{O}_3$  in addition to rhombohedral  $\text{CrRhO}_3$  as confirmed in the XRD patterns (Fig. 1).

Turnover frequency (TOF), a fundamental indicator reflecting the intrinsic catalytic activity and efficiency of a reaction, serves as an important parameter for evaluating electrocatalyst performance. To effectively compare the catalytic activities of  $\text{RhO}_y$  and  $\text{Cr}_x\text{Rh}_{2-x}\text{O}_3\text{-T}$  catalysts,  $\text{TOF}_{\text{metal}}$  (considering Cr and Rh as active sites) was calculated (Fig. S9 and Table S7). Among all the  $\text{Cr}_x\text{Rh}_{2-x}\text{O}_3\text{-T}$  catalysts and  $\text{RhO}_y$ ,  $\text{Cr}_x\text{Rh}_{2-x}\text{O}_3\text{-450}$  showed the highest  $\text{TOF}_{\text{metal}}$  ( $0.030 \text{ s}^{-1}$ ) value at  $\eta =$

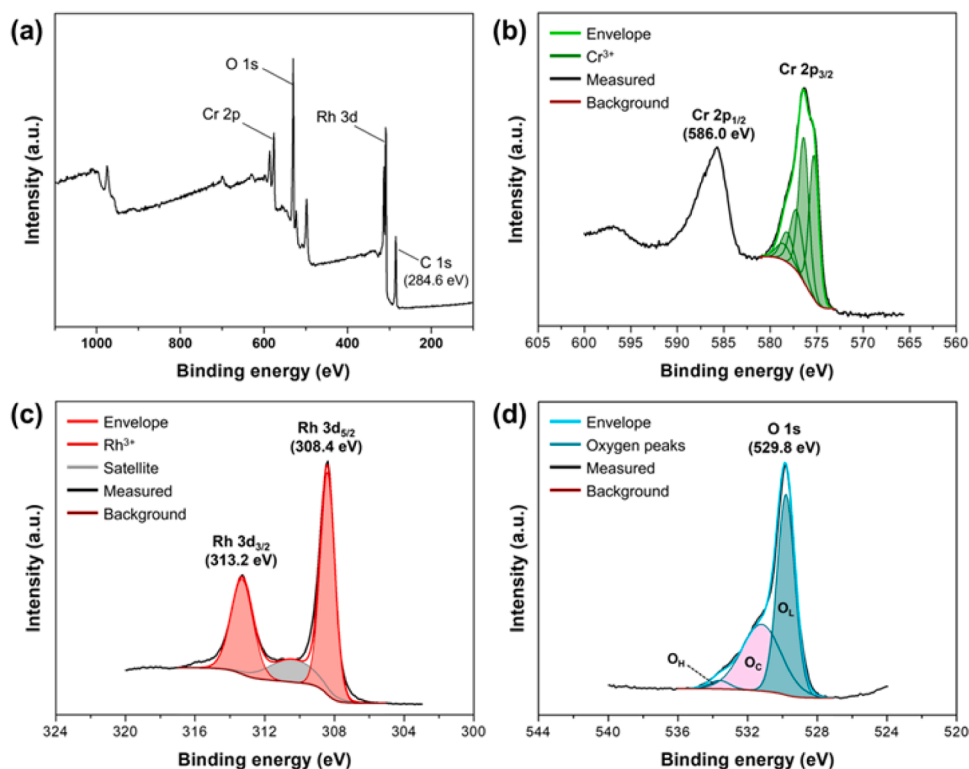


Fig. 4. (a) Survey XPS spectrum, (b) high resolution Cr 2p XPS spectrum, (c) high resolution Rh 3d XPS spectrum, and (d) high resolution O 1s XPS spectrum of single-phase  $\text{Cr}_x\text{Rh}_{2-x}\text{O}_3\text{-450}$ .

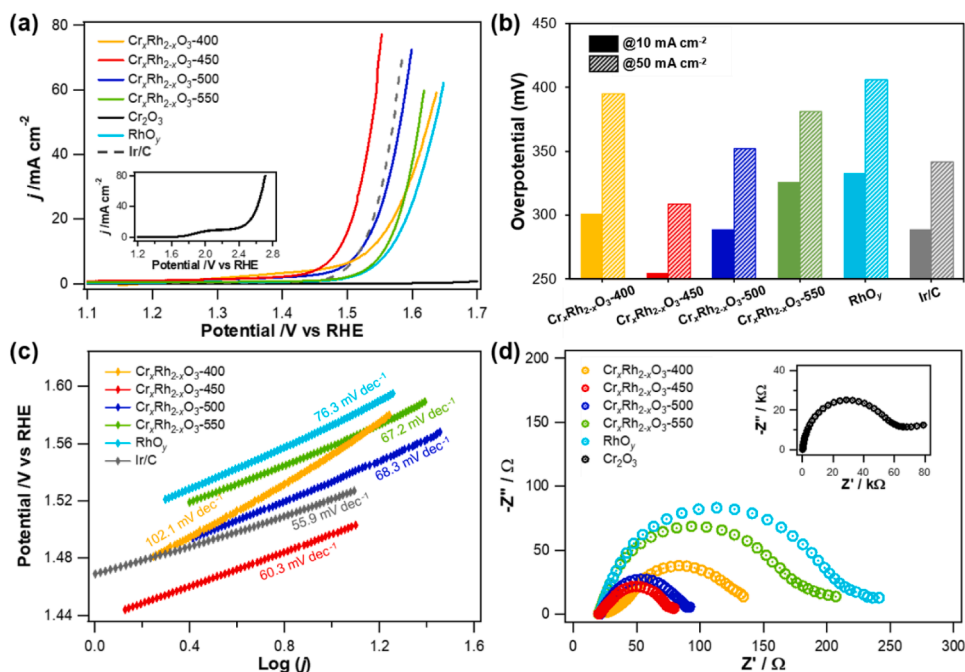


Fig. 5. Electrochemical measurements of  $\text{Cr}_x\text{Rh}_{2-x}\text{O}_3\text{-T}$ ,  $\text{Cr}_2\text{O}_3$ ,  $\text{RhO}_y$  and Ir/C in Ar-saturated 1.0 M KOH solution. (a) Polarization curves obtained at a scan rate of  $10 \text{ mV s}^{-2}$  with a rotation speed of 1600 rpm. Inset shows the LSV curve of  $\text{Cr}_2\text{O}_3$ . (b) The histograms of overpotentials at  $10 \text{ mA cm}^{-2}$  (solid-filled) and  $50 \text{ mA cm}^{-2}$  (hatch-filled). (c) The Tafel plots derived from the LSVs recorded at  $1 \text{ mV s}^{-1}$ . (d) Nyquist plots at  $1.517 \text{ V}$  (vs. RHE). Inset: plot for  $\text{Cr}_2\text{O}_3$ .

$310 \text{ mV}$ . This value was approximately 7-fold higher than  $\text{TOF}_{\text{metal}}$  of  $\text{RhO}_y$  ( $0.0042 \text{ s}^{-1}$ ). Thus,  $\text{Cr}_x\text{Rh}_{2-x}\text{O}_3\text{-450}$  demonstrates significantly enhanced catalytic efficiency for the oxygen evolution reaction (OER) relative to other  $\text{Cr}_x\text{Rh}_{2-x}\text{O}_3\text{-T}$  catalysts and  $\text{RhO}_y$ , consistent with other electrochemical analyses.

To investigate the intrinsic activity of the catalysts more equitably [60], the mass activity of each material (at  $1.54 \text{ V}$  vs RHE) was calculated based on a precious metal, Rh, content. In Fig. S10,  $\text{Cr}_x\text{Rh}_{2-x}\text{O}_3\text{-450}$  displayed a mass activity of  $149 \text{ mA mg}_{\text{Rh}}^{-1}$ , 19-fold higher than that of  $\text{RhO}_y$  ( $8 \text{ mA mg}_{\text{Rh}}^{-1}$ ). In comparison to  $\text{RhO}_y$ ,

$\text{Cr}_x\text{Rh}_{3-x}\text{O}_3$ -450 exhibited higher OER activity with greatly reduced amount of noble Rh, indicating its beneficial features as an economic and excellent OER catalyst.

EIS measurements were performed for the catalyst materials during OER process. Nyquist plots in Fig. 5d presented a semicircle for each of the materials at an applied potential of 1.517 V (vs RHE), which was well fitted with a simple equivalent electrical circuit consisted of three components: solution resistance ( $R_s$ ), charge transfer resistance ( $R_{ct}$ ), and double layer capacitance ( $C_{dl}$ ) [61,62]. Actual  $R_{ct}$  values for

$\text{Cr}_x\text{Rh}_{2-x}\text{O}_3$ - $T$  materials varied remarkably depending on the annealing temperature. In particular,  $R_{ct}$  of  $\text{Cr}_x\text{Rh}_{2-x}\text{O}_3$ -450 was  $57.2 \Omega$ , obviously smaller than that of the other  $\text{Cr}_x\text{Rh}_{2-x}\text{O}_3$ - $T$  nanofibers ( $T = 400, 500$  and  $550$ ) as well as  $\text{RhO}_y$  and  $\text{Cr}_2\text{O}_3$  (Table S8). The smallest  $R_{ct}$  value implies the enhanced conductivity and rapid charge transfer capability of  $\text{Cr}_x\text{Rh}_{2-x}\text{O}_3$ -450 possibly attributed to the elaborate construction of single-phase rhombohedral  $\text{CrRhO}_3$ .

Electrochemically active surface area (ECSA) is an important indicator of OER activity, which is associated with the actual active sites for

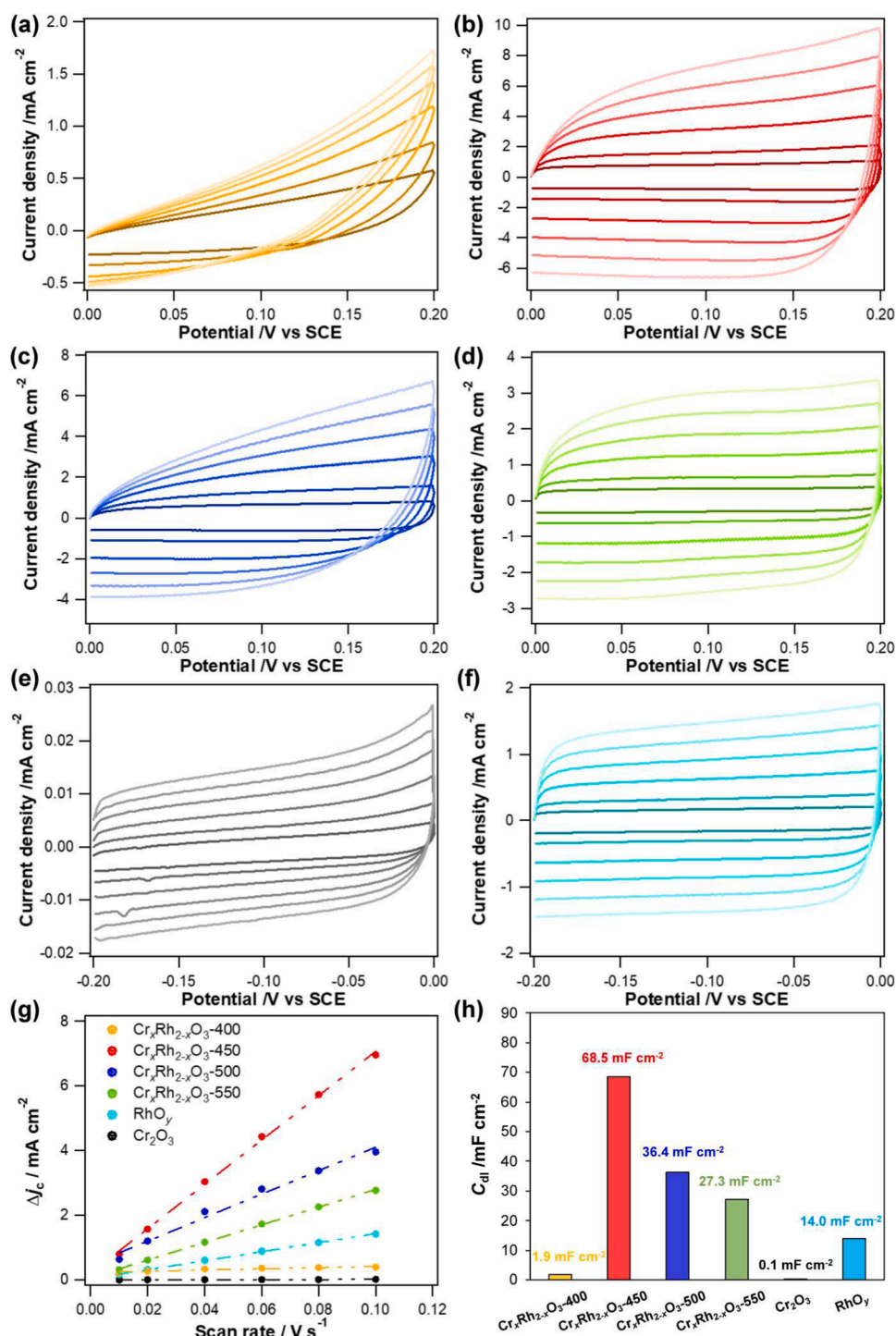


**Fig. 6.** Cyclic voltammograms of the (a)  $\text{Cr}_x\text{Rh}_{2-x}\text{O}_3$ -400, (b)  $\text{Cr}_x\text{Rh}_{2-x}\text{O}_3$ -450, (c)  $\text{Cr}_x\text{Rh}_{2-x}\text{O}_3$ -500, (d)  $\text{Cr}_x\text{Rh}_{2-x}\text{O}_3$ -550, (e)  $\text{RhO}_y$  and (f)  $\text{Cr}_2\text{O}_3$  in 1.0 M KOH (aq) solution at various scan rates (10, 20, 40, 60, 80, and 100  $\text{mV s}^{-1}$ ) with a potential width of 0.2 V. (g) Plots of absolute charging current density ( $\Delta j_c$ ) at the midpoint of the potential range against scan rate and (h) the corresponding  $C_{dl}$  values normalized to geometric surface area.

electrocatalytic reactions [63,64]. Because  $C_{dl}$  is generally assumed to be positively proportional to ECSA, capacitive currents were measured in a non-faradaic potential region of each material with varying potential scan rate. In Fig. 6, all the materials showed the absolute charging current density ( $\Delta j_c$ ) at the midpoint of the potential range linearly proportional to scan rate ( $R^2 > 0.99$ ), except  $\text{Cr}_x\text{Rh}_{2-x}\text{O}_3$ -400 (Fig. 6g). Non-ideal behavior of  $\text{Cr}_x\text{Rh}_{2-x}\text{O}_3$ -400 could be attributed to the low ECSA/conductivity induced by carbon residues from incomplete combustion of PVP as aforementioned. As shown in Fig. 6g and 6h,  $\text{Cr}_x\text{Rh}_{2-x}\text{O}_3$ -450 exhibited the greatest slope of  $\Delta j_c$  vs scan rate corresponding to the largest  $C_{dl}$  value ( $68.5 \text{ mF cm}^{-2}$ ) among all the samples. The smallest  $C_{dl}$  value of  $\text{Cr}_2\text{O}_3$  revealed the presence of few electrochemical active sites and thus demonstrated the poor activity of  $\text{Cr}_2\text{O}_3$  during the OER activity. ECSA of  $\text{Cr}_x\text{Rh}_{2-x}\text{O}_3$ -450 larger than those of  $\text{Cr}_x\text{Rh}_{2-x}\text{O}_3$ -500 and  $\text{Cr}_x\text{Rh}_{2-x}\text{O}_3$ -550 is reasonable because the pore sizes within  $\text{Cr}_x\text{Rh}_{2-x}\text{O}_3$ -T structures increase at the calcination temperature  $\geq 450$  as discussed above regarding the morphological differences based on the TEM images (Fig. S4 and S5). In short, the formation of single  $\text{CrRhO}_3$  phase and appropriate degree of porosity, causing the optimum synergistic effect of Cr and Rh and enlarged ECSA, were harmonized to induce the superior OER activity of  $\text{Cr}_x\text{Rh}_{2-x}\text{O}_3$ -450 even utilizing less than half of noble Rh content compared to pure  $\text{RhO}_y$ . Of importance, the introduction of Cr to Rh made it possible to produce the single-phase rhombohedral  $\text{CrRhO}_3$  possessing the optimum crystallite size (in turn, pore size). Note that  $\text{RhO}_y$ , obtained from pure Rh precursor under the same synthetic condition, possessed mixed phases of rhombohedral and orthorhombic  $\text{Rh}_2\text{O}_3$  with metallic Rh. In fact,  $\text{Cr}_x\text{Rh}_{2-x}\text{O}_3$ -450 even exhibits outstanding performances compared to other Rh-related catalysts reported to date in alkaline media (Table 1) [23,48,65–73].

**Table 1**

Comparison of the OER performances of  $\text{Cr}_x\text{Rh}_{2-x}\text{O}_3$ -450 with other previously reported Rh-related materials in alkaline media.

| Catalyst  | Electrolyte | $\eta_{10}$ (mV)     | Tafel slope (mV dec <sup>-1</sup> ) | Long-term stability test | Ref.      |
|---|-------------|----------------------|-------------------------------------|--------------------------|-----------|
| <sup>a</sup> $\text{Cr}_x\text{Rh}_{2-x}\text{O}_3$ -450  | 1.0 M KOH   | 255                  | 60.3                                | <sup>i</sup> 24 h        | This work |
| <sup>a</sup> $\text{Co}_2\text{RhO}_4$                    | 1.0 M NaOH  | 289                  | 66.5                                | <sup>k</sup> 10 000 s    | [22]      |
| <sup>a</sup> $\text{Ni}_{0.77}\text{Rh}_{0.23}\text{O}_y$ | 1.0 M NaOH  | 310                  | 53.7                                | <sup>k</sup> 10 000 s    | [47]      |
| <sup>b</sup> NiFeRh-LDH                                   | 1.0 M KOH   | 275                  | 29.0                                | <sup>k</sup> 48 h        | [64]      |
| <sup>c</sup> Fe,Rh-Ni <sub>2</sub> P/NF                   | 1.0 M KOH   | 226 @ <sub>j30</sub> | 52.7                                | <sup>k</sup> 24 h        | [65]      |
| <sup>d</sup> Rh-Pt-B                                      | 1.0 M KOH   | 326                  | 82.0                                | –                        | [66]      |
| <sup>e</sup> $\text{Co}_{1.75}\text{Rh}_{0.25}\text{P}$   | 1.0 M KOH   | 290                  | 31.0                                | <sup>l</sup> 50 h        | [67]      |
| <sup>f</sup> Rh/SWNTs                                     | 1.0 M KOH   | 320                  | 89                                  | <sup>l</sup> 10 000 s    | [68]      |
| <sup>g</sup> RhTF_ITO                                     | 1.0 M KOH   | 273                  | 33.56                               | <sup>l</sup> 10 h        | [69]      |
| <sup>h</sup> $\text{Ni}_{1.75}\text{Rh}_{0.25}\text{P}$   | 1.0 M KOH   | 273.1                | 30.0                                | <sup>m</sup> 10 h        | [70]      |
| <sup>i</sup> Rh/CoAl-150 LDH                              | 1.0 M KOH   | 381@ <sub>j100</sub> | 75.0                                | <sup>n</sup> 20 h        | [71]      |
| <sup>j</sup> Rh(20)@Co                                    | 1.0 M KOH   | 310                  | 56.0                                | –                        | [72]      |

<sup>a</sup> Nanofibers,.

<sup>b</sup> Rh-doped NiFe-layered double hydroxide nanosheets,.

<sup>c</sup> Fe,Rh-codoped Ni<sub>2</sub>P nanosheets on nickel foam,.

<sup>d</sup> boron-modified RhPt nanoparticles,.

<sup>e</sup> nanoparticles,.

<sup>f</sup> Rh nanoparticles on single-walled carbon nanotubes,.

<sup>g</sup> seaweed like metallic Rh TF through AACVD method.

<sup>h</sup> Ni<sub>1.75</sub>Rh<sub>0.25</sub>P nanoparticles,.

<sup>i</sup> Rh/CoAl LDH grown on Ni foam,.

<sup>j</sup> fast galvanic displacement of Co by Rh.

<sup>k</sup> Stability test through chronopotentiometry at  $10 \text{ mA cm}^{-2}$ , stability test through chronoamperometry at.

<sup>l</sup> 1.57 V vs. RHE,.

<sup>m</sup> 1.5 V vs. RHE, and.

<sup>n</sup> 1.78 V vs. RHE.

To investigate the stabilities of  $\text{Cr}_x\text{Rh}_{2-x}\text{O}_3$ -450,  $\text{RhO}_y$  and Ir/C in the OER catalysis, chronopotentiometric measurements were conducted. As shown in Fig. 7a,  $\text{Cr}_x\text{Rh}_{2-x}\text{O}_3$ -450 achieved a stabilized overpotential to preserve the catalytic current density of  $10 \text{ mA cm}^{-2}$ , suggesting its outstanding stability for at least 24 h. There was also no significant difference in the LSV polarization curves before and after a 24-h OER for  $\text{Cr}_x\text{Rh}_{2-x}\text{O}_3$ -450. The OER activity of Ir/C was sharply deteriorated after about 10-h OER. Meanwhile, the potential of  $\text{RhO}_y$  remained up to 16 h, then started to increase rapidly after 20 h. This demonstrates that the presence of Cr certainly contributes to the improved long-term durability of  $\text{Cr}_x\text{Rh}_{2-x}\text{O}_3$ -450. The stability of  $\text{Cr}_x\text{Rh}_{2-x}\text{O}_3$ -450 was compared with previously reported Rh-related materials in alkaline media in Table 1. The high stability of  $\text{Cr}_x\text{Rh}_{2-x}\text{O}_3$ -450 was also confirmed with SEM, TEM images and XRD patterns after 24-h stability test, where no morphology or crystallinity change were observed (Fig. S11 and S12). Furthermore, to demonstrate the extended stability, chronopotentiometry was conducted for 48 h (Fig. S13). After the 48-h durability test, the observed potential shift was only approximately 100 mV. Additionally, XRD, SEM, and EDS analyses conducted post-testing revealed no notable changes in the morphology or composition of the catalyst, further highlighting the exceptional durability of  $\text{Cr}_x\text{Rh}_{2-x}\text{O}_3$ -450 (Fig. S14 and Table S9).

### 3.3. DFT analysis

DFT calculations on the electronic properties of the catalyst aid in identifying the catalytic activity and active sites of the catalyst. The structural models were designed in accordance with XRD analysis results. Thermodynamic stability of a catalyst can be determined by computing the formation energy. The calculated formation energy values are summarized in Table S10. All the values for  $\text{Cr}_2\text{O}_3$ ,  $\text{Rh}_2\text{O}_3$  and  $\text{CrRhO}_3$  are negative, indicating that they can be readily synthesized in terms of thermodynamic stability. Furthermore, the formation energy values of  $\text{Cr}_2\text{O}_3$  and  $\text{CrRhO}_3$  are lesser than those of  $\text{Rh}_2\text{O}_3$  in bulk and surface states, as shown in Fig. S15 and Table S10. Understanding the electronic structure of a material is crucial to determining its electron transfer properties, as well as its catalytic origins. Fig. S16 depicts the density of states (DOS) for the catalysts. Since the DOS around Fermi level is a critical parameter to estimate the electrical conductivity, herein the  $\text{CrRhO}_3$  shows higher DOS near the Fermi level compared to  $\text{Cr}_2\text{O}_3$  and  $\text{Rh}_2\text{O}_3$ , implying higher conductivity. Additionally, the partial density of states (PDOS) were analyzed to enumerate the conductivity around Fermi level. To forecast the catalytic activity, the *d*-band center theory has been established [74,75]. According to *d*-band theory, the metal-adsorbate interaction strength is estimated by determining the position of the *d* band center relative to the Fermi level ( $E_F$ ). Also, the filling in a metallic environment is determined by the position of *d* states close to the  $E_F$ . Bonding states are typically filled because their energy states are much lower than  $E_F$ , whereas the electron filling of antibonding states is dependent on these energy states relative to the  $E_F$  and contributes to bond strength [76].

The *d*-band center ( $\epsilon_d$ ) model would be a good descriptor of the metal interaction because the energy of antibonding states is generally higher than that of *d* states [36]. The PDOS of the catalyst was demonstrated in Fig. 8a–c and Fig. S17, where the *d*-orbital of  $\text{CrRhO}_3$  was closer to the Fermi level for the promising catalyst with  $\epsilon_d = -0.021 \text{ eV}$ , whereas  $\text{Cr}_2\text{O}_3$  and  $\text{Rh}_2\text{O}_3$  had the  $\epsilon_d$  values located farther from  $E_F$ , with  $\epsilon_d = 0.297 \text{ eV}$  and  $-1.668 \text{ eV}$ , respectively. The location of the  $\epsilon_d$  in  $\text{CrRhO}_3$  is advantageous to increase the conductivity and capacity for the adsorption of intermediates during the OER process.

J. K. Nørskov *et al.* proposed a four-electron-based OER mechanism [77]; herein, we used it to plot the free energy diagram shown in Fig. 8d–f and the \*OH, \*O, and \*OOH adsorption structures of  $\text{Cr}_2\text{O}_3$ ,  $\text{CrRhO}_3$  and  $\text{Rh}_2\text{O}_3$  were demonstrated in Fig. S18–S20. We obtained theoretical overpotential ( $\eta$ ) on the different active sites of each catalyst. In particular,  $\text{CrRhO}_3$  has a very small  $\eta$  (0.39 V) at the "Cr" site, and it is

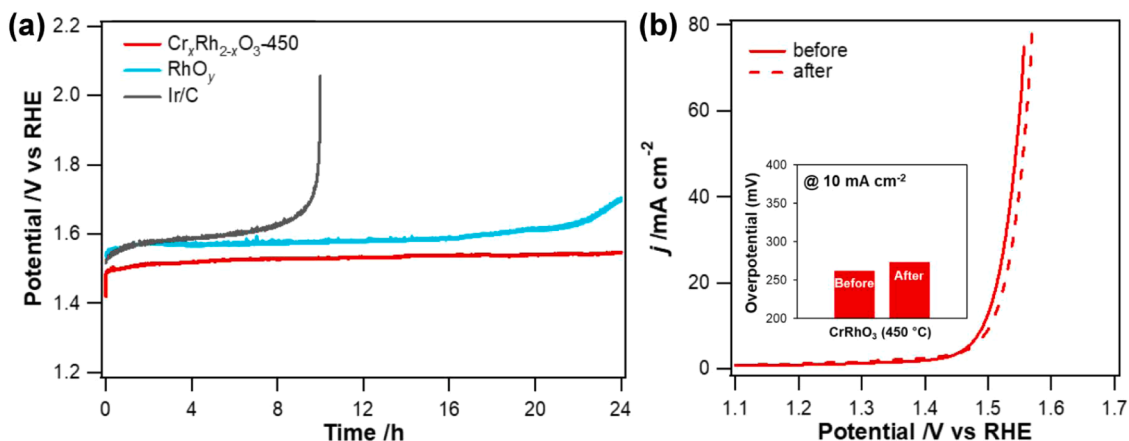


Fig. 7. (a) The chronopotentiometric plot of  $\text{Cr}_x\text{Rh}_{2-x}\text{O}_3$ -450,  $\text{RhO}_y$  and Ir/C collected at  $10 \text{ mA cm}^{-2}$  for 24 h in 1.0 M KOH without  $iR$ -correction. (b) LSV curves of  $\text{Cr}_x\text{Rh}_{2-x}\text{O}_3$ -450 before and after a continuous OER operation for 24 h. The inset shows the corresponding overpotentials at a current density of  $10 \text{ mA cm}^{-2}$ .

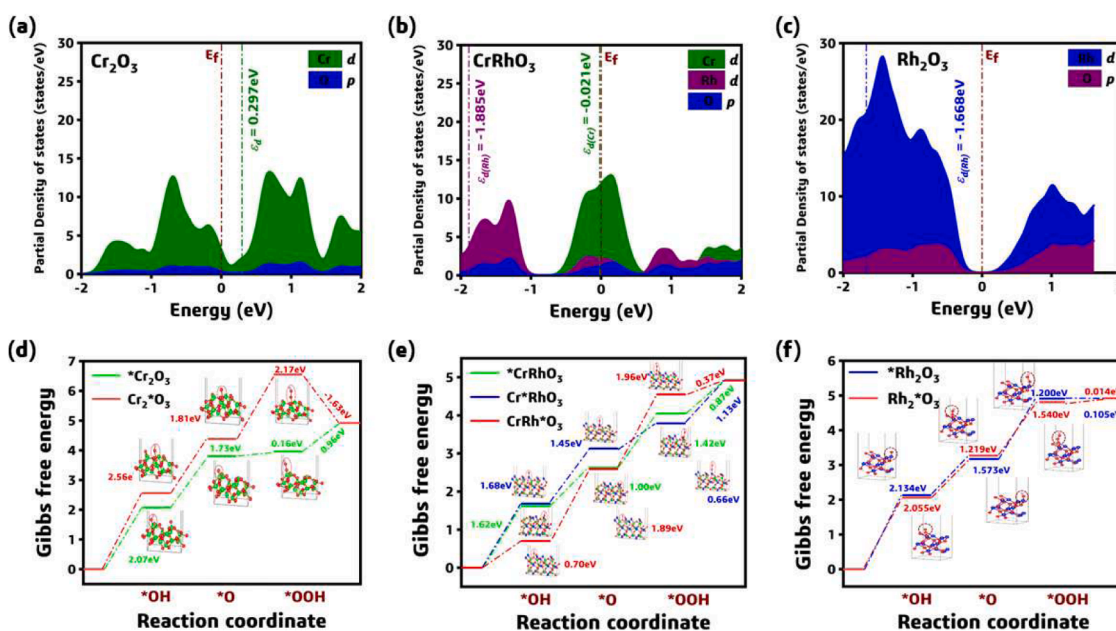


Fig. 8. (a-c) partial density of states (PDOS) of each catalyst with its d-band center ( $\epsilon_d$ ) concerning the Fermi level ( $E_F$ ), and (d-f) OER free energy diagram of  $\text{Cr}_2\text{O}_3$ ,  $\text{CrRhO}_3$ , and  $\text{Rh}_2\text{O}_3$ , respectively.

even smaller than that of commercial catalyst  $\text{RuO}_2$  ( $\eta = 0.42 \text{ V}$ ) [77]. It is noticeable that the "Cr" site acts as a better OER site than "Rh" in the  $\text{CrRhO}_3$  catalyst. As seen in XPS analysis (Fig. S7), the incorporation of Rh ions perturbs the electronic structure of Cr ions by attracting electron density toward Rh ions. This electronic interaction within the rhombohedral  $\text{CrRhO}_3$  structure renders Cr ions relatively more electron-deficient, which may facilitate their adsorption with oxygen-related intermediates of OER. As a result, the alloying effect synergistically enhances catalytic activity by lowering the energy barrier for OER and promoting favorable reaction kinetics on the catalyst surface.

Moreover, the first step (formation of  $^*\text{OH}$ ) has the maximum Gibbs free energy barrier in the reaction pathway at  $^*\text{Cr} = 1.62 \text{ eV}$  and  $^*\text{Rh} = 1.68 \text{ eV}$  of  $\text{CrRhO}_3$ , mainly due to the relatively weaker binding of the oxygen to the catalyst at the stage. Furthermore, the comparative catalyst still has a higher energy barrier with higher  $\eta$  than the optimal catalyst as shown in Table S11. As discussed above,  $\text{CrRhO}_3$  has the  $\epsilon_d$  value of  $-0.021 \text{ eV}$ , which lies closer to the Fermi level and is associated with a lower Gibbs energy barrier for  $\text{OH}^-$  adsorption ( $1.62 \text{ eV}$ )

compared with  $\text{Rh}_2\text{O}_3$  or  $\text{Cr}_2\text{O}_3$ . This implies that tuning the  $\epsilon_d$  closer to the Fermi level can enhance adsorption capacity in the rate-determining step of the OER pathway. OER at "Cr" and "O" in  $\text{Cr}_2\text{O}_3$  has high  $\eta$  values of  $0.84 \text{ V}$  and  $1.33 \text{ eV}$ , respectively, whereas  $\text{Rh}_2\text{O}_3$  outcomes with  $\eta$  values of  $0.90 \text{ V}$  ("Rh") and  $0.83 \text{ V}$  ("O"), respectively. The relationship between theoretical  $\eta$  vs.  $\epsilon_d$  value for each catalyst is shown in Fig. S21. The optimal  $\epsilon_d$  is around  $-0.021 \text{ eV}$  for  $\text{CrRhO}_3$ , which is close to zero; The  $\epsilon_d$  located at too low or too high energy level is detrimental to the OER process. According to the Sabatier principle, the reaction intermediates' moderate adsorption and desorption energies are crucial for catalytic efficiency [78,79]. The OER catalytic activity for  $\text{Cr}_2\text{O}_3$  and  $\text{Rh}_2\text{O}_3$  is restricted by poor bonding to the intermediates caused by  $\epsilon_d$  energy levels that are far from the Fermi level. The bond strength between the surface of  $\text{CrRhO}_3$  and the intermediates are appropriately modulated by the electrons at antibonding states as  $\epsilon_d$  energy levels increase. Therefore, the synergetic effect of "Cr" and "Rh" alters the energy level and improves catalytic activity by lowering the energy barrier and enabling favourable oxygen evolution on the catalyst surface. The improved electrocatalytic activity observed in the

experimental measurement was supported by these DFT results.

#### 4. Conclusions

Single-phase rhombohedral  $\text{Cr}_x\text{Rh}_{2-x}\text{O}_3$  nanofibers were synthesized with electrospinning followed by calcination at a conditioned temperature. In particular, annealing at 450 °C produced highly porous nanofibers composed of optimal  $\text{Cr}_x\text{Rh}_{2-x}\text{O}_3$  crystallites, allowing the best synergistic effect of Cr and Rh; increasing the ECSA greatly; and eventually resulting in the superior OER catalytic performances. Furthermore, theoretical calculations achieved a comprehensive knowledge of the inherent high electroactivity  $\text{CrRhO}_3$  from the perspective of *d*-band centers. Calculations results reveal that  $\text{CrRhO}_3$  can enhance the  $\epsilon_d$  energy level and facilitate OER intermediates' (\*OH, \*O, and \*OOH) adsorption on the catalyst surface, resulting in the lowest theoretical overpotential.

#### CRediT authorship contribution statement

**Taehui Kwon:** Writing – original draft, Visualization, Validation, Methodology, Investigation, Data curation. **Kyungmin Kim:** Visualization, Methodology, Investigation, Data curation. **Sampath Prabhakaran:** Visualization, Software, Methodology, Investigation, Data curation. **Subin Choi:** Validation, Methodology, Investigation, Data curation. **Jiwon Kim:** Methodology, Investigation, Data curation. **Yeji Yim:** Methodology, Data curation. **Jihyun Park:** Methodology, Data curation. **Hoi Ri Moon:** Methodology, Investigation. **Myung Hwa Kim:** Writing – review & editing, Supervision, Resources, Funding acquisition, Conceptualization. **Do Hwan Kim:** Writing – review & editing, Supervision, Software, Funding acquisition, Conceptualization. **Youngmi Lee:** Writing – review & editing, Writing – original draft, Supervision, Resources, Project administration, Funding acquisition, Conceptualization.

#### Declaration of competing interest

The authors declare that they have no known competing financial interests or personal relationships that could have appeared to influence the work reported in this paper.

#### Acknowledgments

This work was financially supported by the National Research Foundation of Korea (NRF) funded by the Ministry of Science and ICT or by the Ministry of Education (NRF-RS-2018-NR031064, NRF-RS-2023-NR076977, NRF-RS-2023-00252880, and NRF-2019R1A5A8080326).

#### Supplementary materials

Supplementary material associated with this article can be found, in the online version, at [doi:10.1016/j.apsadv.2025.100789](https://doi.org/10.1016/j.apsadv.2025.100789).

#### Data availability

Data will be made available on request.

#### References

- [1] F.A. Lattief, M.J. Jweeg, H.S. Majdi, F.A.M. Al-Qrimli, Modeling of electrocatalytic hydrogen evolution via high voltage alkaline electrolyzer with different nanoelectrocatalysts, *Int. J. Hydrog. Energy* 51 (2024) 78–90, <https://doi.org/10.1016/j.ijhydene.2023.08.062>.
- [2] S. Anwar, F. Khan, Y. Zhang, A. Djire, Recent development in electrocatalysts for hydrogen production through water electrolysis, *Int. J. Hydrog. Energy* 46 (2021) 32284–32317, <https://doi.org/10.1016/j.ijhydene.2021.06.191>.
- [3] R. Ding, J. Chen, Y. Chen, J. Liu, Y. Bando, X. Wang, Unlocking the potential: machine learning applications in electrocatalyst design for electrochemical hydrogen energy transformation, *Chem. Soc. Rev.* 53 (2024) 11390–11461, <https://doi.org/10.1039/D4CS00844H>.
- [4] N. Wen, X. Jiao, Y. Xia, D. Chen, Electrocatalysts for the oxygen evolution reaction: mechanism, innovative strategies, and beyond, *Mater. Chem. Front.* 7 (2023) 4833–4864, <https://doi.org/10.1039/D3QM00423F>.
- [5] Q. Shi, C. Zhu, D. Du, Y. Lin, Robust noble metal-based electrocatalysts for oxygen evolution reaction, *Chem. Soc. Rev.* 48 (2019) 3181–3192, <https://doi.org/10.1039/C8CS00671G>.
- [6] C. Hu, L. Zhang, J. Gong, Recent progress made in the mechanism comprehension and design of electrocatalysts for alkaline water splitting, *Energy Environ. Sci.* 12 (2019) 2620–2645, <https://doi.org/10.1039/C9EE01202H>.
- [7] X. Zhang, R. Xu, T. Wang, L. Niu, Y. Gong, C. Li, Enhancing electrocatalytic performance in the oxygen evolution reaction of zirconium-based amorphous high-entropy oxides via controlled introduction of oxygen vacancies: experimental insights and DFT simulations, *J. Colloid Interface Sci.* 694 (2025) 137635, <https://doi.org/10.1016/j.jcis.2025.137635>.
- [8] H. Yang, X. Han, A.L. Douka, L. Huang, L. Gong, C. Xia, H.S. Park, B.Y. Xia, Advanced oxygen electrocatalysis in energy conversion and storage, *Adv. Funct. Mater.* 31 (2021) 2007602, <https://doi.org/10.1002/adfm.202007602>.
- [9] R. Qin, G. Chen, X. Feng, J. Weng, Y. Han, Ru/Ir-based electrocatalysts for oxygen evolution reaction in acidic conditions: from mechanisms, optimizations to challenges, *Adv. Sci.* 11 (2024) 2309364, <https://doi.org/10.1002/advs.202309364>.
- [10] W. Zhu, X. Song, F. Liao, H. Huang, Q. Shao, K. Feng, Y. Zhou, M. Ma, J. Wu, H. Yang, H. Yang, M. Wang, J. Shi, J. Zhong, T. Cheng, M. Shao, Y. Liu, Z. Kang, Stable and oxidative charged Ru enhance the acidic oxygen evolution reaction activity in two-dimensional ruthenium-iridium oxide, *Nat. Commun.* 14 (2023) 5365, <https://doi.org/10.1038/s41467-023-41036-9>.
- [11] M.A. Hubert, A.M. Patel, A. Gallo, Y. Liu, E. Valle, M. Ben-Naim, J. Sanchez, D. Sokaras, R. Sinclair, J.K. Nørskov, L.A. King, M. Bajdich, T.F. Jaramillo, Acidic oxygen evolution reaction activity–Stability relationships in Ru-based pyrochlores, *ACS Catal.* 10 (2020) 12182–12196, <https://doi.org/10.1021/acscatal.0c02252>.
- [12] S. Czioska, A. Boubnov, D. Escalera-López, J. Geppert, A. Zagalskaya, P. Röse, E. Saraçi, V. Alexandrov, U. Krewer, S. Cherevko, J.-D. Grunwaldt, Increased Ir–Ir interaction in iridium oxide during the oxygen evolution reaction at high potentials probed by operando spectroscopy, *ACS Catal.* 11 (2021) 10043–10057, <https://doi.org/10.1021/acscatal.1c02074>.
- [13] H.-S. Park, J. Yang, M.K. Cho, Y. Lee, S. Cho, S.-D. Yim, B.-S. Kim, J.H. Jang, H.-K. Song, RuO<sub>2</sub> nanocluster as a 4-in-1 electrocatalyst for hydrogen and oxygen electrochemistry, *Nano Energy* 55 (2019) 49–58, <https://doi.org/10.1016/j.nanoen.2018.10.01>.
- [14] Y. Pi, Y. Xu, L. Li, T. Sun, B. Huang, L. Bu, Y. Ma, Z. Hu, C.W. Pao, X. Huang, Selective surface reconstruction of a defective iridium-based catalyst for high-efficiency water splitting, *Adv. Funct. Mater.* 30 (2020) 2004375, <https://doi.org/10.1002/adfm.202004375>.
- [15] D.F. Abbott, L. Lebedev, K. Waltar, M. Povia, M. Nachttegaal, E. Fabbri, C. Copéret, T.J. Schmidt, Iridium oxide for the oxygen evolution reaction: correlation between particle size, morphology, and the surface hydroxyl layer from operando XAS, *Chem. Mat.* 28 (2016) 6591–6604, <https://doi.org/10.1021/acs.chemmater.6b02625>.
- [16] H. Jin, Y. Hong, J. Yoon, A. Oh, N.K. Chaudhari, H. Baik, S.H. Joo, K. Lee, Lanthanide metal-assisted synthesis of rhombic dodecahedral MnI (M = Ir and Pt) nanoframes toward efficient oxygen evolution catalysis, *Nano Energy* 42 (2017) 17–25, <https://doi.org/10.1016/j.nanoen.2017.10.033>.
- [17] K. Shen, T. Wang, C. Li, M. Chen, L. Niu, Y. Gong, Designing highly-efficient oxygen evolution reaction FeCoNiCrMnO<sub>x</sub> electrocatalyst via coexisted crystalline and amorphous phases: experiment and theory, *Appl. Surf. Sci.* 650 (2024) 159102, <https://doi.org/10.1016/j.apsusc.2023.159102>.
- [18] J.-Y. Zhu, Q. Xue, Y.-Y. Xue, Y. Ding, F.-M. Li, P. Jin, P. Chen, Y. Chen, Iridium nanotubes as bifunctional electrocatalysts for oxygen evolution and nitrate reduction reactions, *ACS Appl. Mater. Interfaces* 12 (2020) 14064–14070, <https://doi.org/10.1021/acscami.0c01937>.
- [19] J. Lim, D. Park, S.S. Jeon, C.W. Roh, J. Choi, D. Yoon, M. Park, H. Jung, H. Lee, Ultrathin IrO<sub>2</sub> nanoneedles for electrochemical water oxidation, *Adv. Funct. Mater.* 28 (2018) 1704796, <https://doi.org/10.1002/adfm.201704796>.
- [20] B. Jiang, Y. Guo, J. Kim, A.E. Whitten, K. Wood, K. Kani, A.E. Rowan, J. Henzie, Y. Yamauchi, Mesoporous metallic iridium nanosheets, *J. Am. Chem. Soc.* 140 (2018) 12434–12441, <https://doi.org/10.1021/jacs.8b05206>.
- [21] X. Kong, K. Xu, C. Zhang, J. Dai, S. Norooz Oliaee, L. Li, X. Zeng, C. Wu, Z. Peng, Free-standing two-dimensional Ru nanosheets with high activity toward water splitting, *ACS Catal.* 6 (2016) 1487–1492, <https://doi.org/10.1021/acscatal.5b02730>.
- [22] J. Ruiz Esquivias, G. Algara-Siller, I. Spanos, S.J. Freakley, R. Schlögl, G. J. Hutchings, Preparation of solid solution and layered IrO<sub>x</sub>–Ni(OH)<sub>2</sub> oxygen evolution catalysts: toward optimizing iridium efficiency for OER, *ACS Catal.* 10 (2020) 14640–14648, <https://doi.org/10.1021/acscatal.0c03866>.
- [23] S.Y. Kim, A. Yu, Y. Lee, H.Y. Kim, Y.J. Kim, N.-S. Lee, C. Lee, Y. Lee, M.H. Kim, Single phase of spinel Co<sub>2</sub>RhO<sub>4</sub> nanotubes with remarkably enhanced catalytic performance for the oxygen evolution reaction, *Nanoscale* 11 (2019) 9287–9295, <https://doi.org/10.1039/C9NR02197C>.
- [24] D. Liu, Q. Lv, S. Lu, J. Fang, Y. Zhang, X. Wang, Y. Xue, W. Zhu, Z. Zhuang, IrCuNi deeply concave nanocubes as highly active oxygen evolution reaction electrocatalyst in acid electrolyte, *Nano Lett.* 21 (2021) 2809–2816, <https://doi.org/10.1021/acs.nanolett.0c04878>.
- [25] Y. Lin, Z. Tian, L. Zhang, J. Ma, Z. Jiang, B.J. Deibert, R. Ge, L. Chen, Chromium-ruthenium oxide solid solution electrocatalyst for highly efficient oxygen evolution

- reaction in acidic media, *Nat. Commun.* 10 (2019) 1–13, <https://doi.org/10.1038/s41467-018-08144-3>.
- [26] D. Jin, J. Kang, S. Prabhakaran, Y. Lee, M.H. Kim, D.H. Kim, C. Lee, Chromium-rich  $\text{Cr}_x\text{Fe}_{1-x}\text{O}_2$  tube-in-tube alloys for boosted water oxidation with long standing electrocatalytic activity, *J. Mater. Chem. A* (2022), <https://doi.org/10.1039/D2TA02984G>.
- [27] N. Du, C. Wang, X. Wang, Y. Lin, J. Jiang, Y. Xiong, Trimetallic TriStar nanostructures: tuning electronic and surface structures for enhanced electrocatalytic hydrogen evolution, *Adv. Mater.* 28 (2016) 2077–2084, <https://doi.org/10.1002/adma.201504785>.
- [28] Z. Sun, M. Yuan, H. Yang, L. Lin, H. Jiang, S. Ge, H. Li, G. Sun, S. Ma, X. Yang, 3D porous amorphous  $\gamma\text{-CrOOH}$  on Ni foam as bifunctional electrocatalyst for overall water splitting, *Inorg. Chem.* 58 (2019) 4014–4018, <https://doi.org/10.1021/acs.inorgchem.9b00112>.
- [29] P. Kim, A. Anderko, A. Navrotsky, R.E. Riman, Trends in structure and thermodynamic properties of normal rare earth carbonates and rare earth hydroxycarbonates, *Minerals* 8 (2018) 106, <https://doi.org/10.3390/min8030106>.
- [30] J. Ekspong, T. Wågberg, Stainless steel as a bi-functional electrocatalyst—A top-down approach, *Materials (Basel)* 12 (2019) 2128, <https://doi.org/10.3390/ma12132128>.
- [31] S. Anantharaj, M. Venkatesh, A.S. Salunke, T.V. Simha, V. Prabu, S. Kundu, High-performance oxygen evolution anode from stainless steel via controlled surface oxidation and Cr removal, *ACS Sustain. Chem. Eng.* 5 (2017) 10072–10083, <https://doi.org/10.1021/acssuschemeng.7b02090>.
- [32] W. Gou, M. Zhang, Y. Zou, X. Zhou, Y. Qu, Iridium-chromium oxide nanowires as highly performed OER catalysts in acidic media, *Chem. Cat. Chem.* 11 (2019) 6008–6014, <https://doi.org/10.1002/cctc.201901411>.
- [33] L. Ma, X. Shi, X. Zhang, L. Li, Electrospinning of polycaprolactone/chitosan core-shell nanofibers by a stable emulsion system, *J. Colloid. Interface Sci.* 583 (2019) 123956, <https://doi.org/10.1016/j.cis.2019.123956>.
- [34] Y. Nam, D. Jin, S. Choi, D.H. Hong, H.R. Moon, Y. Lee, Lotus-root-like multichannel nanotubes of  $\text{IrO}_2\text{-ZnO}$  for electrocatalysis of pH-universal oxygen evolution reaction: a simple strategy to control the structure and crystallinity, *Appl. Surf. Sci.* 644 (2024) 158741, <https://doi.org/10.1016/j.apsusc.2023.158741>.
- [35] Z. Zhang, X. Wu, Z. Kou, N. Song, G. Nie, C. Wang, F. Verpoort, S. Mu, Rational design of electrospun nanofiber-typed electrocatalysts for water splitting: a review, *Chem. Eng. J.* 428 (2022) 131133, <https://doi.org/10.1016/j.cej.2021.131133>.
- [36] S. Sun, X. Zhou, B. Cong, W. Hong, G. Chen, Tailoring the d-band centers endows  $(\text{Ni}_x\text{Fe}_{1-x})_2\text{P}$  nanosheets with efficient oxygen evolution catalysis, *ACS Catal* 10 (2020) 9086–9097, <https://doi.org/10.1021/acscatal.0c01273>.
- [37] J.H. Shim, J. Kim, C. Lee, Y. Lee, Electrocatalytic activity of gold and gold nanoparticles improved by electrochemical pretreatment, *J. Phys. Chem. C* 115 (2011) 305–309, <https://doi.org/10.1021/jp1067507>.
- [38] E. Skúlason, V. Tripkovic, M.E. Björketun, S. Gudmundsdóttir, G. Karlberg, J. Rossmeisl, T. Bligaard, H. Jónsson, J.K. Nørskov, Modeling the electrochemical hydrogen oxidation and evolution reactions on the basis of density functional theory calculations, *J. Phys. Chem. C* 114 (2010) 18182–18197, <https://doi.org/10.1021/jp1048887>.
- [39] Z. Wang, H. Liu, R. Ge, X. Ren, J. Ren, D. Yang, L. Zhang, X. Sun, Phosphorus-doped  $\text{Co}_3\text{O}_4$  nanowire array: a highly efficient bifunctional electrocatalyst for overall water splitting, *ACS Catal* 8 (2018) 2236–2241, <https://doi.org/10.1021/acscatal.7b03594>.
- [40] K. Momma, F. Izumi, VESTA 3 for three-dimensional visualization of crystal, volumetric and morphology data, *J. Appl. Crystallogr.* 44 (2011) 1272–1276, <https://doi.org/10.1107/S0021889811038970>.
- [41] P.E. Blöchl, O. Jepsen, O.K. Andersen, Improved tetrahedron method for Brillouin-zone integrations, *Phys. Rev. B* 49 (1994) 16223, <https://doi.org/10.1103/PhysRevB.49.16223>.
- [42] A.S. Botana, M.R. Norman, Electronic structure and magnetism of transition metal dihalides: bulk to monolayer, *Phys. Rev. Mater.* 3 (2019) 044001, <https://doi.org/10.1103/PhysRevMaterials.3.044001>.
- [43] G. Kresse, J. Hafner, Norm-conserving and ultrasoft pseudopotentials for first-row and transition elements, *J. Phys.-Condens. Matter* 6 (1994) 8245, <https://doi.org/10.1088/0953-8984/6/40/015>.
- [44] A. Pandey, S. Dalal, S. Dutta, A. Dixit, Structural characterization of polycrystalline thin films by X-ray diffraction techniques, *J. Mater. Sci.-Mater. Electron.* 32 (2021) 1341–1368, <https://doi.org/10.1007/s10854-020-04998-w>.
- [45] J. Xie, J. Zhang, S. Li, F. Grote, X. Zhang, H. Zhang, R. Wang, Y. Lei, B. Pan, Y. Xie, Controllable disorder engineering in oxygen-incorporated  $\text{MoS}_2$  ultrathin nanosheets for efficient hydrogen evolution, *J. Am. Chem. Soc.* 135 (2013) 17881–17888, <https://doi.org/10.1021/ja408329q>.
- [46] Y. Zhu, H.A. Tahini, Y. Wang, Q. Lin, Y. Liang, C.M. Doherty, Y. Liu, X. Li, J. Lu, S. C. Smith, Pyrite-type ruthenium disulfide with tunable disorder and defects enables ultra-efficient overall water splitting, *J. Mater. Chem. A* 7 (2019) 14222–14232, <https://doi.org/10.1039/C9TA04120F>.
- [47] P. Barpanda, N. Recham, J.-N. Chotard, K. Djellab, W. Walker, M. Armand, J.-M. Tarascon, Structure and electrochemical properties of novel mixed Li ( $\text{Fe}_{1-x}\text{M}_x$ ) $\text{SO}_4\text{F}$  ( $\text{M} = \text{Co}, \text{Ni}, \text{Mn}$ ) phases fabricated by low temperature ionothermal synthesis, *J. Mater. Chem.* 20 (2010) 1659–1668, <https://doi.org/10.1039/B922063A>.
- [48] D. Jin, A. Yu, Y. Lee, M.H. Kim, C. Lee,  $\text{Ni}_x\text{Rh}_{1-x}\text{O}_y$  composite nanofibres as highly efficient and robust oxygen evolution electrocatalysts, *J. Alloy. Compd.* 836 (2020) 155309, <https://doi.org/10.1016/j.jallcom.2020.155309>.
- [49] Z. Dai, F. Qin, H. Zhao, J. Ding, Y. Liu, R. Chen, Crystal defect engineering of aurivillius  $\text{Bi}_2\text{MoO}_6$  by Ce doping for increased reactive species production in photocatalysis, *ACS Catal* 6 (2016) 3180–3192, <https://doi.org/10.1021/acscatal.6b00490>.
- [50] J. Jiang, F. Sun, S. Zhou, W. Hu, H. Zhang, J. Dong, Z. Jiang, J. Zhao, J. Li, W. Yan, Atomic-level insight into super-efficient electrocatalytic oxygen evolution on iron and vanadium co-doped nickel (oxy) hydroxide, *Nat. Commun.* 9 (2018) 1–12, <https://doi.org/10.1038/s41467-018-05341-y>.
- [51] B.J. Rani, B. Saravanakumar, G. Ravi, V. Ganesh, A. Sakunthala, R. Yuvakkumar, Structural, optical and magnetic properties of NiO nanopowders, *J. Nanosci. Nanotechnol.* 18 (2018) 4658–4666, <https://doi.org/10.1166/jnn.2018.15301>.
- [52] D. Khanolkar, Crystal structure data of some rhodites and ruthenites, *Curr. Sci.* 30 (1961) 52–53.
- [53] J. Mackolil, B. Mahanthesh, Sensitivity analysis of Marangoni convection in  $\text{TiO}_2\text{-EG}$  nanoliquid with nanoparticle aggregation and temperature-dependent surface tension, *J. Therm. Anal. Calorim.* 143 (2021) 2085–2098, <https://doi.org/10.1007/s10973-020-09642-7>.
- [54] D. Zhen, B. Zhao, H.C. Shin, Y. Bu, Y. Ding, G. He, M. Liu, Electrospun porous perovskite  $\text{La}_{0.6}\text{Sr}_{0.4}\text{Co}_{1-x}\text{Fe}_x\text{O}_{3-\delta}$  nanofibers for efficient oxygen evolution reaction, *J. Therm. Anal. Calorim.* 4 (2017) 1700146, <https://doi.org/10.1002/admi.201700146>.
- [55] M.C. Biesinger, B.P. Payne, A.P. Grosvenor, L.W. Lau, A.R. Gerson, R.S.C. Smart, Resolving surface chemical states in XPS analysis of first row transition metals, oxides and hydroxides: cr, Mn, Fe, Co and Ni, *Appl. Surf. Sci.* 257 (2011) 2717–2730, <https://doi.org/10.1016/j.apsusc.2010.10.051>.
- [56] M. Biesinger, C. Brown, J. Mycroft, R. Davidson, N. McIntyre, X-ray photoelectron spectroscopy studies of chromium compounds, *Surf. Interface Anal.* 36 (2004) 1550–1563, <https://doi.org/10.1002/sia.1983>.
- [57] J. Bai, S.-H. Han, R.-L. Peng, J.-H. Zeng, J.-X. Jiang, Y. Chen, Ultrathin rhodium oxide nanosheet nanoassemblies: synthesis, morphological stability, and electrocatalytic application, *ACS Appl. Mater. Interfaces* 9 (2017) 17195–17200, <https://doi.org/10.1021/acsami.7b04874>.
- [58] T. Cottre, M. Fingerle, M. Kranz, T. Mayer, B. Kaiser, W. Jaegermann, Interaction of water with atomic layer deposited titanium dioxide on p-Si photocathode: modeling of photoelectrochemical interfaces in ultrahigh vacuum with cryo-photoelectron spectroscopy, *J. Therm. Anal. Calorim.* 8 (2021) 2002257, <https://doi.org/10.1002/admi.202002257>.
- [59] T. Shinagawa, A.T. Garcia-Esparza, K. Takanebe, Insight on Tafel slopes from a microkinetic analysis of aqueous electrocatalysis for energy conversion, *Sci. Rep.* 5 (2015) 1–21, <https://doi.org/10.1038/srep13801>.
- [60] C. Wei, Z.J. Xu, The Comprehensive Understanding of As an Evaluation Parameter for Electrochemical Water Splitting, Wiley Online Library, 2018 1800168, <https://doi.org/10.1002/smt.201800168>.
- [61] D.A. Harrington, P. Van Den Driessche, Mechanism and equivalent circuits in electrochemical impedance spectroscopy, *Electrochim. Acta* 56 (2011) 8005–8013, <https://doi.org/10.1016/j.electacta.2011.01.067>.
- [62] J.-M. Hu, J.-Q. Zhang, C.-N. Cao, Oxygen evolution reaction on  $\text{IrO}_2$ -based DSA® type electrodes: kinetics analysis of Tafel lines and EIS, *Int. J. Hydrog. Energy* 29 (2004) 791–797, <https://doi.org/10.1016/j.ijhydene.2003.09.007>.
- [63] P. Connor, J. Schuch, B. Kaiser, W. Jaegermann, The determination of electrochemical active surface area and specific capacity revisited for the system  $\text{MnO}_x$  as an oxygen evolution catalyst, *S. Phys. Chem.* 234 (2020) 979–994, <https://doi.org/10.1515/zpch-2019-1514>.
- [64] S. Li, R. Feng, M. Li, X. Zhao, B. Zhang, Y. Liang, H. Ning, J. Wang, C. Wang, P. K. Chu, Needle-like  $\text{CoO}$  nanowire composites with NiO nanosheets on carbon cloth for hybrid flexible supercapacitors and overall water splitting electrodes, *RSC Adv.* 10 (2020) 37489–37499, <https://doi.org/10.1039/D0RA07307E>.
- [65] H. Sun, W. Zhang, J.-G. Li, Z. Li, X. Ao, K.-H. Xue, K.K. Ostrikov, J. Tang, C. Wang, Rh-engineered ultrathin NiFe-LDH nanosheets enable highly-efficient overall water splitting and urea electrolysis, *Appl. Catal. B-Environ.* 284 (2021) 119740, <https://doi.org/10.1016/j.apcatb.2020.119740>.
- [66] M.-T. Chen, J.-J. Duan, J.-J. Feng, L.-P. Mei, Y. Jiao, L. Zhang, A.-J. Wang, Iron, rhodium-codoped  $\text{Ni}_2\text{P}$  nanosheets arrays supported on nickel foam as an efficient bifunctional electrocatalyst for overall water splitting, *J. Colloid Interface Sci.* 605 (2022) 888–896, <https://doi.org/10.1016/j.jcis.2021.07.101>.
- [67] Y. Wang, W. Guo, Z. Zhu, K. Xu, H. Zhang, W. Wei, X. Xiao, W. Liang, M. He, T. Yu, Interfacial boron modification on mesoporous octahedral rhodium shell and its enhanced electrocatalysis for water splitting and oxygen reduction, *Chem. Eng. J.* 435 (2022) 134982, <https://doi.org/10.1016/j.cej.2022.134982>.
- [68] S.I. Mutinda, D. Li, J. Kay, S.L. Brock, Synthesis and characterization of  $\text{Co}_{2-x}\text{Rh}_x\text{P}$  nanoparticles and their catalytic activity towards the oxygen evolution reaction, *J. Mater. Chem. A* 6 (2018) 12142–12152, <https://doi.org/10.1039/C8TA02016G>.
- [69] W. Zhang, X. Zhang, L. Chen, J. Dai, Y. Ding, L. Ji, J. Zhao, M. Yan, F. Yang, C.-R. Chang, Single-walled carbon nanotube induced optimized electron polarization of rhodium nanocrystals to develop an interface catalyst for highly efficient electrocatalysis, *ACS Catal* 8 (2018) 8092–8099, <https://doi.org/10.1021/acscatal.8b02016>.
- [70] M.M. Hasan, T. Islam, S.S. Shah, M.A. Aziz, A. Awal, M.D. Hossain, M.A. Ehsan, A. J.S. Ahmamd, Supporting electrolyte interaction with the AACVD synthesized Rh thin film influences the OER activity, *Int. J. Hydrog. Energy* 47 (2022) 28740–28751, <https://doi.org/10.1016/j.ijhydene.2022.06.212>.
- [71] T.N. Batugedara, S.L. Brock, Role of noble- and base-metal speciation and surface segregation in  $\text{Ni}_{2-x}\text{Rh}_x\text{P}$  nanocrystals on electrocatalytic water splitting reactions in alkaline Media, *Chem. Mat.* 34 (2022) 4414–4427, <https://doi.org/10.1021/acs.chemmat.2c00041>.
- [72] Y. Li, X. Wang, X. Han, S. Yin, J. Xia, Assembly engineering of Rh atoms on CoAl-layered double hydroxide nanosheets for boosting alkaline water splitting, *ACS*

- Appl. Nano Mater. 6 (2023) 7984–7991, <https://doi.org/10.1021/acsanm.3c01222>.
- [73] B. Nedić Vasiljević, A.Z. Jovanović, S.V. Mentus, N.V. Skorodumova, I.A. Pašti, Galvanic displacement of Co with Rh boosts hydrogen and oxygen evolution reactions in alkaline media, *J. Solid State Electrochem.* 27 (2023) 1877–1887, <https://doi.org/10.1007/s10008-023-05374-4>.
- [74] T. Bligaard, J.K. Nørskov, Ligand effects in heterogeneous catalysis and electrochemistry, *Electrochim. Acta* 52 (2007) 5512–5516, <https://doi.org/10.1016/j.electacta.2007.02.041>.
- [75] H. Jin, X. Liu, S. Chen, A. Vasileff, L. Li, Y. Jiao, L. Song, Y. Zheng, S.-Z. Qiao, Heteroatom-doped transition metal electrocatalysts for hydrogen evolution reaction, *ACS Energy Lett* 4 (2019) 805–810, <https://doi.org/10.1021/acsenergylett.9b00348>.
- [76] Z. Chen, Y. Song, J. Cai, X. Zheng, D. Han, Y. Wu, Y. Zang, S. Niu, Y. Liu, J. Zhu, Tailoring the d-band centers enables Co<sub>4</sub>N nanosheets to be highly active for hydrogen evolution catalysis, *Angew. Chem.* 130 (2018) 5170–5174, <https://doi.org/10.1002/anie.201801834>.
- [77] I.C. Man, H.Y. Su, F. Calle-Vallejo, H.A. Hansen, J.I. Martínez, N.G. Inoglu, J. Kitchin, T.F. Jaramillo, J.K. Nørskov, J. Rossmeisl, Universality in oxygen evolution electrocatalysis on oxide surfaces, *Chem. Cat. Chem.* 3 (2011) 1159–1165, <https://doi.org/10.1002/cctc.201000397>.
- [78] J. Yan, L. Kong, Y. Ji, J. White, Y. Li, J. Zhang, P. An, S. Liu, S.-T. Lee, T. Ma, Single atom tungsten doped ultrathin  $\alpha$ -Ni(OH)<sub>2</sub> for enhanced electrocatalytic water oxidation, *Nat. Commun.* 10 (2019) 1–10, <https://doi.org/10.1038/s41467-019-09845-z>.
- [79] V.R. Stamenkovic, B.S. Mun, M. Arenz, K.J. Mayrhofer, C.A. Lucas, G. Wang, P. N. Ross, N.M. Markovic, Trends in electrocatalysis on extended and nanoscale Pt-bimetallic alloy surfaces, *Nat. Mater.* 6 (2007) 241–247, <https://doi.org/10.1038/nmat1840>.